

1 **A global estimate of monthly vegetation and soil fractions from**
2 **spatio-temporally adaptive spectral mixture analysis during 2001-**
3 **2022**

4 Qiangqiang Sun¹, Ping Zhang², Xin Jiao¹, Xin Lin¹, Wenkai Duan³, Su Ma⁴, Qidi Pan¹, Lu Chen¹,
5 Yongxiang Zhang¹, Shucheng You⁵, Shunxi Liu⁶, Jinmin Hao¹, Hong Li^{7*}, Danfeng Sun^{1,8*}

6 ¹College of Land Science and Technology, China Agricultural University, Beijing, 100193, China

7 ²National Geomatics Center of China, Beijing, China.

8 ³China Agricultural University Library, China Agricultural University, Beijing, 100193, China

9 ⁴Chinese Research Academy of Environmental Sciences, Beijing, China

10 ⁵Land Satellite Remote Sensing Application Center, Ministry of Natural Resources, Beijing, China

11 ⁶China Land Survey and Planning Institute, Ministry of Natural Resources, Beijing, China

12 ⁷Institute of plant nutrition and resources, Beijing Academy of Agriculture and Forestry Sciences, Beijing, China

13 ⁸Technology innovation Center of land engineering, Ministry of Natural Resources, Beijing, China

14
15 *Correspondence to:* Danfeng Sun (sundf@cau.edu.cn); Hong Li (lih5176@126.com)

31 **Abstract.** Multifaceted regime shifts of Earth’s surface are ongoing dramatically and—in turn—considerably alter global
32 carbon budget, energy balance and biogeochemical cycles. Sustainably managing terrestrial ecosystems necessitates a
33 deeper comprehension of the diverse and dynamic nature of multi-component information within these environments.
34 However, comprehensive records of global-scale fractional vegetation and soil information that encompass these structural
35 and functional complexities remain limited. Here, we provide a globally comprehensive record of monthly vegetation and
36 soil fractions during the period 2001–2022 using a spatio-temporally adaptive spectral mixture analysis framework. This
37 product is designed to continuously represent Earth's terrestrial surface as a percentage of five physically meaningful
38 vegetation and soil endmembers, including photosynthetic vegetation (PV), non-photosynthetic vegetation (NPV), bare
39 soil (BS), ice/snow (IS), and dark surface (DA), with high accuracy and low uncertainty, compared to previous vegetation
40 index and vegetation continuous fields product, as well as traditional fully constrained linear spectral mixture models. We
41 also adopt non-parametric seasonal Mann-Kendall tested fractional dynamics to identify shifts based on interactive changes
42 of these fractions. Our results—superior to previous portrayal of the greening planet—not only report a $+9.35 \times 10^5 \text{ km}^2$
43 change of photosynthetic vegetation, but also explore decrease of non-photosynthetic vegetation ($-2.19 \times 10^5 \text{ km}^2$), bare soil
44 ($-5.14 \times 10^5 \text{ km}^2$), and dark surface ($-2.27 \times 10^5 \text{ km}^2$). Besides, Interactive changes of these fractions yield multifaceted
45 regime shifts with important implications, such as a simultaneous increase in PV and NPV in central and southwest China
46 during afforestation activities, an increase of PV in cropland of China and India due to intensive agricultural development,
47 a decrease of PV and increase of BS in tropical zones resulting from deforestation. These advantages highlight that our
48 dataset which provides locally relevant information on multifaceted regime shifts at the required scale, enabling scalable
49 modelling and effective governance of future terrestrial ecosystems. The data about fractional five surface vegetation and
50 soil components are available on Science Data Bank (<https://doi.org/10.57760/sciencedb.13287>, Sun and Sun, 2023).

51
52
53
54
55
56
57
58

59 **1 Introduction**

60 Global terrestrial ecosystems are experiencing rapid and uncertain climate change and anthropogenic impacts since the
61 twenty-first century (Alkama and Cescatti 2016; IPCC 2013; Song et al. 2018), which have profound impacts on shifts of
62 Earth's surface, such as greening of the planet (Chen et al. 2019; Piao et al. 2006; Zhu et al. 2016), afforestation (Chen et
63 al. 2019; Tong et al. 2018), deforestation (Qin et al. 2019; Zeng et al. 2018), agricultural expansion (Chen et al. 2019; Zeng
64 et al. 2018; Yu et al., 2021), glacier melting (Hugonnet et al., 2021; Zemp et al., 2019; Soheb et al., 2022), and urban sprawl
65 (Kuang et al. 2020; Liu et al. 2020; Zhang et al., 2022). These land surface shifts inversely play a fundamental role in
66 affecting climate change via considerably altering the Earth's carbon budget, energy balance and biogeochemical cycles
67 (Lawrence and Vandecar 2015; Qin et al. 2021). Increased understanding of these land cover changes is urgent requirement
68 (Réjou-Méchain et al., 2021; Liu et al., 2020) to support the scientific, legislative and land management communities who
69 strive to understand locally relevant knowledge and further protect, restore, and promote the sustainable use of terrestrial
70 ecosystems under Sustainable Development Goal.

71 However, land surface interpretation is obstructed by extensive existence of mixed pixels in satellite imagery, especially
72 in heterogeneous landscapes (Roberts et al. 1993). Continuous vegetation indexes (e.g., normalized difference vegetation
73 index (NDVI), enhanced vegetation index (EVI)) provide limited information on surface composition, which hinders our
74 ability of understanding ecosystem's structurally and functionally multifaceted shifts (Smith et al. 2019; Sun 2015; Zeng
75 et al., 2023). In recent years, there have been significant advancements in fractional vegetation cover within the fields of
76 remote sensing and environmental science. This progress has led to the development of various products at multiple
77 resolutions, such as long-term global land surface satellite (GLASS), GEOV Fcover, multi-source data synergized
78 quantitative remote sensing production system (MuSyQ) fractional vegetation cover (Baret et al. 2013; Jia et al., 2015; Mu
79 et al., 2017; Zhao et al., 2023). These products primarily integrate and utilize data from different spectral bands and sensors,
80 employing methods including machine learning, radiative transfer model and dimidiate pixel model (Baret et al. 2013; Yan
81 et al., 2021; Zhao et al., 2023). However, these data primarily focus on green vegetation, posing significant limitations in
82 capturing information regarding non-photosynthetic vegetation and bare soil. In ecological studies and remote sensing,
83 non-photosynthetic vegetation including stems, branches, and other plant structures primarily serve functions other than
84 photosynthesis, such as support and storage. Therefore, understanding the distribution and characteristics of non-
85 photosynthetic vegetation is important for a comprehensive analysis of ecosystems and land cover, especially in drylands
86 (Guerschman et al., 2009). Although some initiatives and products focused on multi-element fractions, such as MOD44B
87 and the Global Vegetation Fractional Cover Product (DiMiceli et al., 2015; Guerschman et al., 2015). For instance, the
88 Global Vegetation Fractional Cover Product primarily targets arid regions, particularly Australia, focusing on

89 photosynthetic vegetation, non-photosynthetic vegetation, and bare soil. Meanwhile, MOD44B achieves global-scale
90 acquisition of trees, non-trees, and non-vegetative cover. There is a lack of unified classification systems among these
91 products across global scale.

92 Previous advances in spectral mixture analysis method have facilitated investigation of estimating physically fractional
93 vegetation and soil information in the mixed pixels with relatively few field points (Roberts et al. 1993; Small 2004; Smith
94 et al. 1990). These unmixed endmember fractions provide multicomponent time series of information on surface
95 heterogeneous composition and interactive evolution rather than individual vegetation indices (Elmore et al. 2000; Franke
96 et al. 2009; Small and Milesi 2013; Sun 2015) and have been adopted to reveal the temporally dynamical systems under
97 the influence of a changing environment and human activity (Lewińska et al. 2020; Suess et al. 2018; Sun et al. 2021).
98 Recent studies have proven that spectral mixture analysis model has the advantage of providing more accurate and
99 physically based representation of fraction vegetation-soil continues field in the subpixel level without training samples
100 (Daldegan et al. 2019; Smith et al. 2007). This measurement offers a continuous, quantitative portrayal of land surface
101 properties instead of discrete land cover classes, as well as superior to many of spectral indexes (e.g., vegetation index)
102 (Rogan et al. 2002; Sun et al. 2019; Sun et al. 2020). Despite extensive validation and application of this method at the
103 regional scale, there remain lack of global records of unmixed fractional vegetation and soil information, which may be
104 resulted from the temporal and spatial variability of global intra-class and inter-class endmember spectra (Wang et al. 2021).
105 Recent advance in endmember variability has verified that Multiple Endmember Spectral Mixture Analysis (MESMA) was
106 recommended be used in most applications considering its robustness in mitigating the endmember variability (Zhang et
107 al., 2019). Such approach is well suited for heterogeneous landscapes because it allows an optimized model with varying
108 the number and types of endmembers within each pixel (Roberts et al. 1998; Franke et al., 2009). However, considering
109 world-wide landscapes with enormous heterogeneity under the climate fluctuations and human activities, the paradox of
110 fine-grained spatial representation and challenged data processing for large scale and long-time series characterization of
111 land surface has not yet been fully solved.

112 Here, we create a unified monthly fractional vegetation-soil nexuses product for the period 2001 to 2021, with an spatio-
113 temporally adaptive MESMA methods at powerful Google Earth Engine (GEE) platform that provide powerful
114 computational processing to realize planetary-scale analysis of geospatial data, at the same scale as monthly composites of
115 MOD43A4 imageries (500×500m spatial resolution). This product is designed to continuously represent Earth's terrestrial
116 surface as a percentage of surface endmembers with standard endmember spectra globally, providing a gradation of five
117 surface vegetation and soil components: photosynthetic vegetation (PV), non-photosynthetic vegetation (NPV), bare soil

118 (BS), ice/snow (IS), and dark surface (DA). And we use non-parametric seasonal Mann-Kendall test to quantify global
119 trends and their interactive shifts in fractional vegetation-soil nexuses over the full period.

120 **2 Materials and methods**

121 **2.1 Dataset**

122 The MCD43A4 Version 6 Nadir Bidirectional Reflectance Distribution Function Adjusted Reflectance (NBAR) product
123 is selected in this study (Schaaf and Wang 2015). Since the view angle effects have been removed from the directional
124 reflectance, this dataset is provided as more stable and consistent daily surface reflectance imageries (bands 1-7) using best
125 representative pixel of 16-day retrieval period of Terra and Aqua spacecrafts at 500-m sinusoidal projection. The
126 MCD43A4 dataset was then temporally aggregated to produce a monthly composited dataset by taking the medium of all
127 valid reflectance in GEE platform during 2001–2022.

128 The Köppen-Geiger climate classification is a reasonable approach to aggregate complex climate gradients into a simple
129 but ecologically meaningful classification scheme (Beck et al. 2018). This dataset presents their widespread acceptance
130 and usage within the scientific community. This classification scheme includes five main classes and 30 subtypes (Beck et
131 al. 2018). We thus selected recently developed global Köppen-Geiger climate classification maps at a 1-km resolution for
132 the present-day (1980–2016). We initially used the 30-subtype classification for the selection of typical regions for the
133 endmembers collection. Meanwhile, we aggregated 30 sub-types to five main classes (i.e., tropical, arid, temperate, cold,
134 and polar) according to classification scheme criteria to represent a static climate condition in this study.

135 The land cover datasets are provided by the collection 6 MODIS land cover products (MCD12Q1) with 500-meter spatial
136 resolution in 2001 and 2022 (Friedl and Sulla-Menashe, 2015). MCD12Q1 utilizes multiple datasets and robust algorithms,
137 and provides detailed and reliable land cover information. It has been proven advantages in representing the global land
138 cover structure, patterns, and dynamics, aligning well with the requirements of our study for endmember selection. We
139 aggregate the International Geosphere-Biosphere Programme (IGBP) classification types of these datasets into three
140 regions—ecological zone, agricultural zone, urbanized zone. We define ecological zone as combination of evergreen
141 needleleaf forest, evergreen broadleaf forest, deciduous needleleaf forest, deciduous broadleaf forest and mixed forest,
142 closed shrublands, open shrublands, woody savannahs, savannahs, grasslands, permanent wetlands, Permanent snow and
143 ice, barren; refine agricultural zone as aggregation of cropland/natural vegetation mosaics; and represent urbanized zone
144 by urban and built-up lands.

145 2.2 Spatio-temporally adaptive spectral mixture analysis

146 Recent advances in spectral mixture analysis methods have facilitated investigation of estimating fractional endmember
147 abundances in the mixed pixels (Meyer and Okin 2015; Okin 2007; Roberts et al. 1993). This method assumes that the
148 reflectance of target mixing pixel is a linear combination of the weighting coefficients (proportional endmembers) and
149 associated pure spectra,

$$150 R_i = \sum_{j=1}^m F_j E_{i,j} + \varepsilon_i \quad (1)$$

151 Where R_i is actual reflectance for band i ; $E_{i,j}$ is the reflectance of a given endmember j ($1 \leq j \leq m$) for a specific band i ; m is
152 the number of endmembers; F_j is fractional abundance of this endmember j ; and ε_i is the residual error for specific band i .
153 The fully constrained least squares spectral mixture analysis model, including abundance sum-to-one constraint and
154 abundance non-negativity constraint, is commonly applied for estimation of fractional endmembers to guarantee physically
155 meaningful results (Heinz and Chein-I-Chang 2002). Spectral mixture analysis model is assessed by the model residual
156 error (ε_i), reported as the root-mean-square-error ($RMSE_{sma}$), which can be expressed as Eq(2):

$$157 RMSE_{sma} = \sqrt{\frac{\sum_{i=1}^n \varepsilon_i^2}{n}} \quad (2)$$

158 The spectral mixture analysis model includes three processes: endmember selection, and fraction estimation, and evaluation.

159 2.2.1 Nested endmember selection considering spatio-temporal variability.

160 The quality of spectral mixture analysis is significantly dependent on the representativeness of endmember selected.
161 Endmember spectra used in spectral mixture analysis, in general, can either be derived from measured field spectral library
162 or images (Franke et al. 2009; Sonnentag et al. 2007). The image-based endmember selection method is more practical
163 way because advantage of image endmember is that they can be collected at the same scale as the image and are relatively
164 easy to associate with image features (Rashed et al. 2003). Given that such endmember selection would be hampered by
165 temporal and spatial variability of global intra-class and inter-class endmember spectra, we develop a nested framework
166 for endmember selection considering spatial and temporal variability (Fig. 1).

167 (1) Recent studies have proposed various compositional endmember frameworks in different application contexts. For
168 example, a framework including substrate, vegetation, dark and ice/snow was proposed and verified globally for both
169 Landsat and MODIS to allow estimated fractions, this framework ensures consistent comparison of estimated fractions
170 across diverse climate patterns and land cover types (Small and Milesi 2013; Sousa and Small 2019). Another framework

171 includes photosynthetic vegetation, non-photosynthetic vegetation, soil, and shade (Roberts et al. 1993), this framework
172 was widely adopted for presentation surface structure worldwide, particularly in tropical rainforest and dryland ecosystems
173 (Guerschman et al., 2015). These elements can characterize the fundamental composition of the Earth surface. Thus, we
174 embody five endmembers to represent surface units, these five endmembers include photosynthetic vegetation (PV), non-
175 photosynthetic vegetation (NPV), bare soil (BS), dark (DA), ice/snow (IS). Concretely, PV refers to green photosynthetic
176 foliage characterized by chlorophyll absorptions in the visible and high reflectance in the near-infrared bands; NPV
177 represents non-tilled cropland/grassland, and tree litters; BS contains soil, rock, and sediment. DA represents a fundamental
178 ambiguity; thus, it may be either absorptive (e.g., black lava), transmissive (e.g., deep clear water) or non-illuminated
179 (shadow) surface. IS is permanent glaciers and snow that are widespread in the polar regions and high mountains.

180 (2) Considering both climate patterns and land cover types, the typical sites employed for standardized endmembers
181 selection were chosen based on global MODIS sinusoidal grid ($10^\circ \times 10^\circ$ intervals). The Köppen-Geiger climate
182 classification zones is adopted as the dominant criterion to undertaking full coverage of climate types (Beck et al. 2018).
183 Meanwhile, we also examine land cover diversity, characterized by Simpson's Diversity Index (D) of recent MCD12Q1
184 Version 6 product in 2020 in each MODIS grid.

$$185 \quad D = 1 - \sum_{i=1}^m (P_i)^2 \quad (3)$$

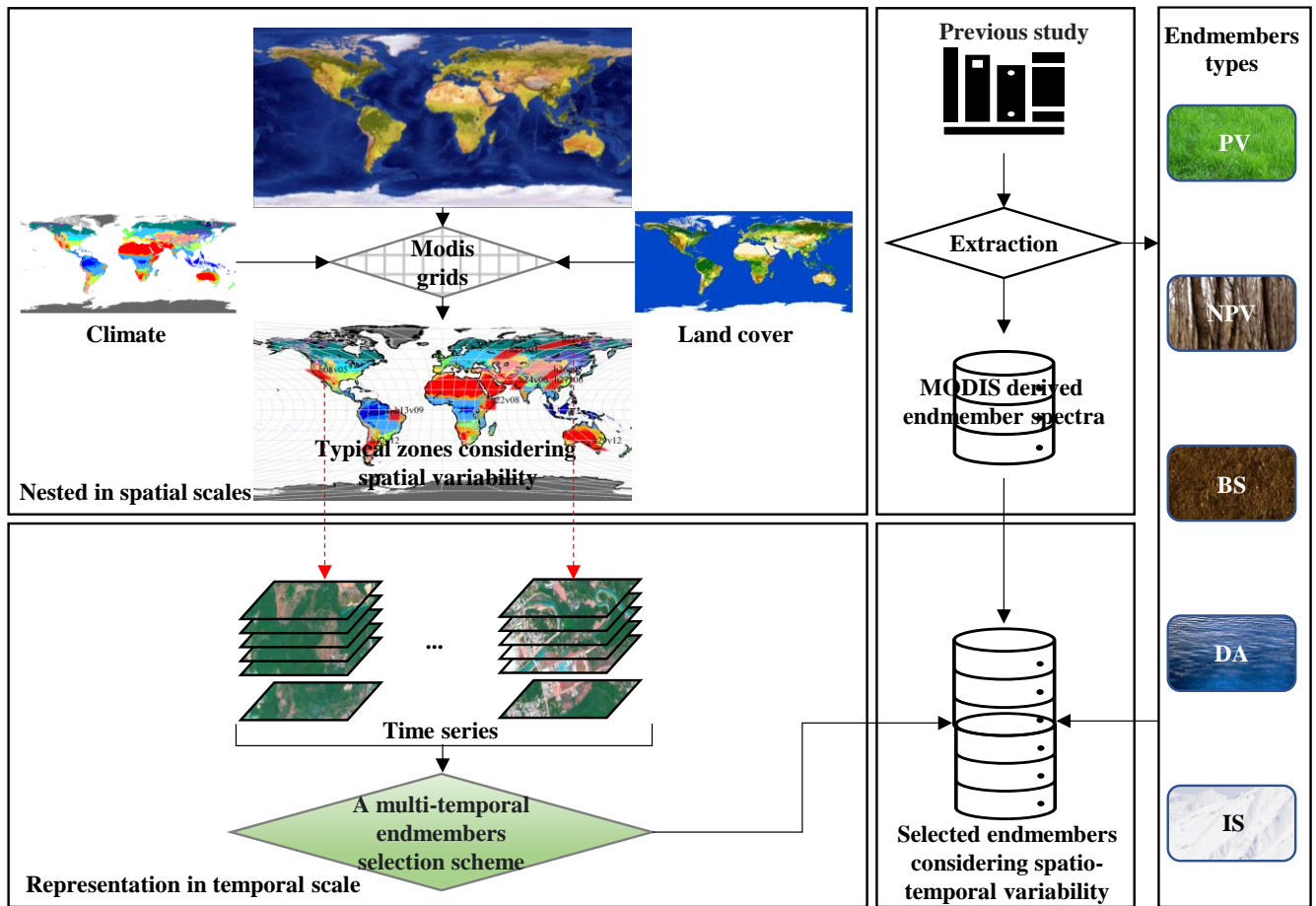
186 Where P_i is percentage of type i land use and cover in the grid, m is number of land use and cover in the grid. Finally, we
187 selected the top 10 grids (i.e., h08v05, h12v12, h13v09, h16v01, h21v03, h22v02, h22v08, h24v06, h26v05, h27v06,
188 h29v12) in terms of Simpson's Diversity Index (D) among all MODIS grids (Fig. S1a, b), and containing all Köppen-
189 Geiger climate types (Fig. S1c), were selected for generation of standardized endmember spectrum.

190 (3) The representativeness of endmembers always shifts with time variation. A multi-temporal endmembers selection
191 scheme has been validated for various time series images (Sun and Liu 2015; Sun et al. 2018). This process of utilization
192 of both spatially and temporally mixed image collections for endmember selection can consider both spatial and temporal
193 variability. Therefore, the multi-temporal standardized endmembers selection scheme is adopted in 10 typical zones that
194 considering both climate and land cover diversity. Principal component (PC) transformation derived eigenvectors and
195 associated PC images were utilized as criteria for determination of endmember types. Specifically, eigenvector of PC,
196 displaying remarkable differences between shortwave infrared bands with other visible and near-infrared bands, is
197 obviously able to highlight characteristics of IS. PC eigenvector with relatively high contrast between the near-infrared
198 band and other bands primarily captures information related to photosynthetic vegetation (PV), particularly during
199 vegetation growing seasons. The BS and NPV will be boosted with the PC when corresponding eigenvector emerges the

200 same direction. Even though there is no obvious regular pattern of eigenvector for DA determination, the PC images can
201 provide adequate information coupled with high-resolution images of Google Earth. After the determination of
202 endmembers type and their PCs in each grid, we ranked these PCs by descending order of the variance contribution, and
203 selected PC images of first three timings for endmember selection. We have listed the endmember types and their
204 highlighting timings for each selected grid in Table S1. The image endmembers can be acquired from the vertex's pixels
205 (200-400 pixels) of scatter plot formed by the PC images at their corresponding timings in each grid. We then exported
206 these acquired pure pixels as regions of interest to compute original MODIS reflectance as endmember spectra. These
207 selected pure pixels for each endmember are validated by high spatial resolution remote sensing imagery of Google Earth
208 (Fig. S2).

209 (4) Besides, we collect MODIS derived endmember spectra used in previous study to complement and enrich the diversity
210 of the spectral library (Okin et al. 2013; Daldegan et al. 2019; Meyer and Okin 2015; Sousa and Small 2019). We gather 7
211 PV, 5 NPV, 5 BS, and 1 DA endmember spectra through such literature search method. Finally, we establish a library of
212 endmember spectra considering spatio-temporal variability, this library includes 35 PV spectra, 40 BS spectra, 25 NPV
213 spectra, 16 DA spectra, and 15 IS spectra.

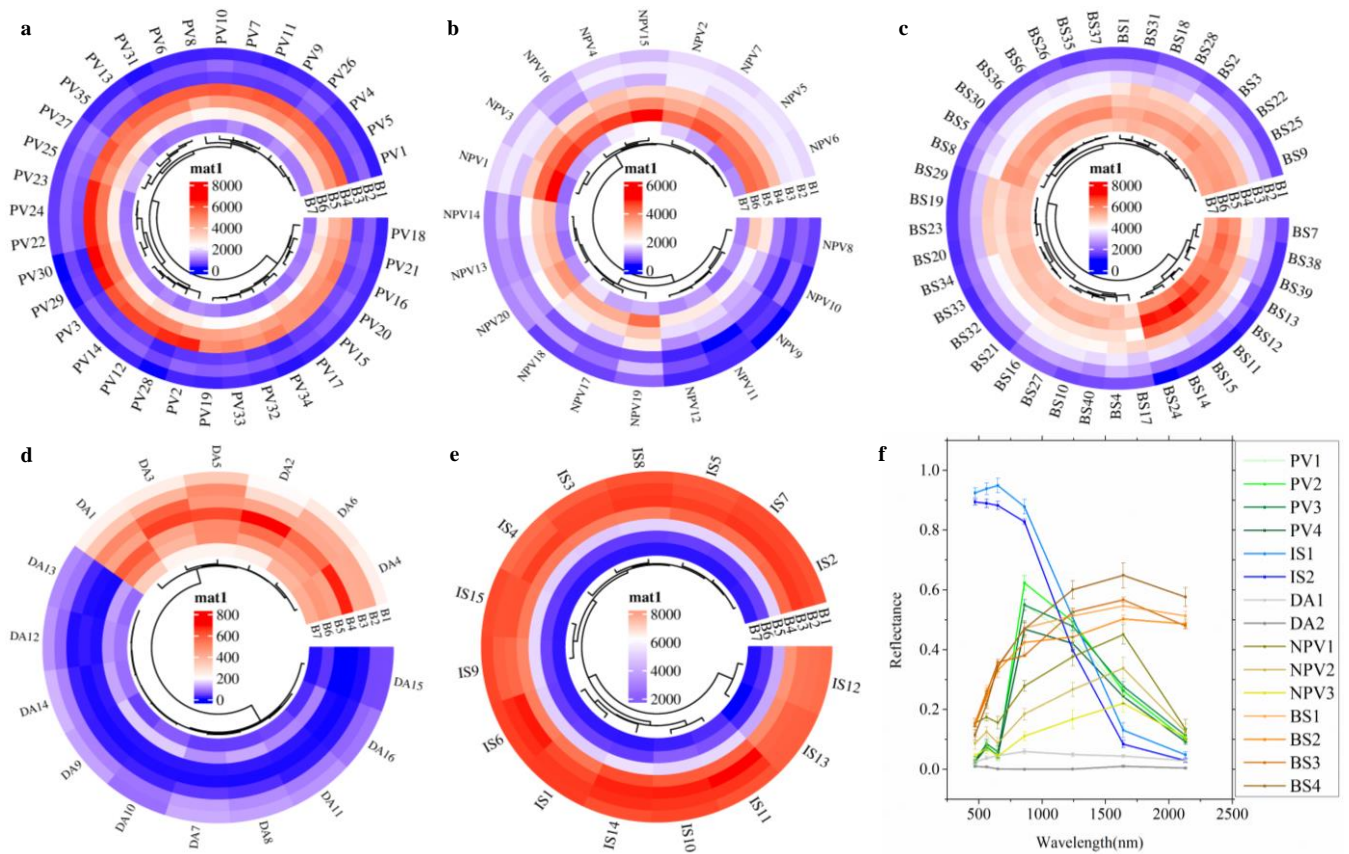
214 (5) To ensure feasibility of pixel-by-pixel operations in GEE, we also consider the similarity between the spectral curves,
215 the hierarchical clustering method is selected to aggregate these spectra of each endmember as sub-groups, we input all
216 spectral curves per endmember, grouping similar curves to compute their mean—a representative typical spectral curve for
217 each cluster. Such hierarchical clustering boasts strong interpretability and adaptability for clustering at diverse scales
218 within data analysis. Finally, we obtain 4 PV spectra, 4 BS spectra, 3 NPV spectra, 2 DA spectra, and 2 IS spectra to
219 estimate vegetation and soil fractions at global scale during 2001 to 2020 (Fig. 2).



220

221

Figure 1: A framework for endmember selection considering spatial and temporal variability.



222

223 **Figure 2: Endmember spectra.** a-e, Hierarchical clusters of the endmember spectra of PV, NPV, BS, DA and IS. f, the
 224 averaged final endmember spectra including 4 PV spectra, 4 BS spectra, 3 NPV spectra, 2 DA spectra, and 2 IS spectra.
 225 B1-B7 represent MODIS spectral bands, including 459-479nm, 545-565nm, 620-670nm, 841-876nm, 1230-1250nm, 1628-
 226 1652nm, and 2105-2155nm.

227 2.2.2 Multiple Endmember Spectral Mixture Analysis

228 The MESMA has been used to estimate fractional vegetation-soil nexuses based on selected endmember spectra. According
 229 to the convex geometry concepts, the number of endmember (n+1) in the model should be equal to the intrinsic
 230 dimensionality of the spectral space (n) plus one (Boardman 2013). We found the cumulative contribution of the top three
 231 PCs has exceeded 99% (Fig. S3), this three-dimensional PC space allows four-endmember models. We initially generate
 232 multiple endmember combinations based on selected endmember spectra, and achieve 692 combination models, including
 233 two-endmember model (88), three-endmember model (252) and four-endmember model (352) (Table S2). The fully

234 constrained least squares spectral mixture analysis model is selected to estimate fractions and count $RMSE_{sma}$ for each
235 endmember combination in GEE platform. We finally search a specific endmember combination with the smallest
236 $RMSE_{sma}$ and achieve the estimated endmember fractions of this combination as final fractions.

237 **2.3 Direct validation of the dataset**

238 The smallest $RMSE_{sma}$ of 692 combination models is adopted as criteria to assess suitability and uncertainty of the model.
239 The model suggests a generally good fit when mean $RMSE_{sma}$ over the image is less than 0.02 (Wu and Murray 2003).
240 Moreover, due to challenges in conducting fraction estimation validation through field surveys, we employ reference data
241 obtained from high spatial resolution images as validation set. We thus select for two sets of reference data that their land
242 cover classification systems are closely related to our five endmembers. Global Land Cover Validation Reference Dataset
243 (GLCVRD) is provided with a 2m reference dataset from very high resolution commercial remote sensing data within $5 \times$
244 5 km blocks from 2003 to 2012 (Olofsson et al. 2012; Pengra et al. 2015; Stehman et al. 2012). These datasets support
245 global estimates of classification accuracy for four major land cover classes: tree, water, barren, other vegetation, cloud,
246 shadow, ice & snow. Various recent studies have selected this dataset to evaluate the continuous fields of land cover types
247 (Baumann et al. 2018; Qin et al. 2019; Song et al. 2018). We use all GLCVRD reference dataset (Fig. 3a) to assess the
248 accuracy of globally fractional vegetation and soil estimates from MESMA. Firstly, we filter the estimated fractions based
249 on the corresponding year and month obtained from the reference data. Simultaneously, aligning the interpretations of land
250 cover types with our endmembers, we pair them accordingly, that is, tree and other vegetation represent PV and NPV,
251 barren stands for BS, water and shadow correspond to DA, and ice & snow denote IS. Subsequently, we reclassify these
252 paired land cover types and calculated their percentage within 5×5 km blocks, in which we exclude cloud coverage (named
253 no data). Additionally, utilizing these cloud-free pixels in each block, we compute the mean of fractional values for each
254 endmember, and then compare these estimated fractions with the measured percentage of paired the reclassified land cover
255 types to validate the reliability of our product (Fig. S4). Based on paired measured fractions and our estimated fractions
256 within blocks, we adopt four accuracy metrics including mean error (ME), mean absolute error (MAE), root-mean-square-
257 error (RMSE), and R^2 for accuracy assessment. ME measures the average of all errors in the dataset where errors are the
258 differences between predicted and actual values, MAE calculates the average of the absolute differences between predicted
259 and actual values, RMSE provides a measure of prediction error, whereas R^2 offers insight into the amount of variability
260 in the dependent variable that the model explains. These metrics provide a more comprehensive assessment of the model's
261 accuracy, helping to understand different facets of its performance, such as bias, variability, and overall predictive power
262 (James et al., 2013).

263
$$ME = \frac{\sum_{i=1}^n (p_i - r_i)}{n} \quad (4)$$

264
$$MAE = \frac{\sum_{i=1}^n |p_i - r_i|}{n} \quad (5)$$

265
$$RMSE = \sqrt{\frac{\sum_{i=1}^n (p_i - r_i)^2}{n}} \quad (6)$$

266
$$R^2 = 1 - \frac{\sum_{i=1}^n (p_i - r_i)^2}{\sum_{i=1}^n (p_i - \bar{r})^2} \quad (7)$$

267 Where p_i , r_i are estimated endmember fractions and reference endmember fractions at i th block, n is sample size ($n = 474$),
 268 \bar{r} is mean of the reference endmember fractions of all blocks.

269 Besides, we also authenticate our product through incorporating comprehensive global land cover and land use reference
 270 data (Fritz et al. 2017), which were obtained from the Geo-Wiki crowdsourcing platform across four campaigns: Human
 271 impact, wilderness, reference and disagreement. Over 150000 samples of land cover and land use were acquired in this
 272 reference data. To effectively validate our product, we need to filter the reference data, considering aspects such as data
 273 acquisition time, measurement methods, and credibility. We select first three campaigns, which have a good match with
 274 MODIS pixels (size 1×1 km) and were observed during 2001 to 2022. High feasibility reference data is then selected
 275 through the confidence information of land cover estimates and the status of use of high spatial resolution imagery provided
 276 by the metadata. Similarly to the procedural description used for fractional vegetation-soil compared to GLCVRD, we
 277 reclassify ten classes of this dataset into our four groups of endmembers, including (1) tree cover, shrub cover, herbaceous
 278 vegetation/grassland, cultivated and managed, and mosaic of cultivated and managed/natural vegetation to PV and NPV;
 279 (2) flooded/wetland and open water to DA; (3) urban and barren to BS; (4) snow and ice to IS. This involve comparing the
 280 measured percent of land cover with the mean of endmember fractions within the corresponding 1×1 km pixels.

281 **2.4 Comparisons and uncertainties analysis**

282 To verify the consistency and merits of our dataset against existing ones, we conducted comparisons with four distinct pre-
 283 existing datasets: NDVI, Leaf area index (LAI), MOD44B Vegetation Continuous Fields product, GLASS fractional
 284 vegetation cover dataset, and GEOV Fcover dataset. NDVI is derived from monthly synthesized MCD43A4 images. **LAI**
 285 **is derived from 8-day composite MOD15A2H V6 dataset at 500m resolution.** Both mean values of NDVI/LAI and our
 286 estimated fractional PV across all years are considered for comparison. The MOD44B Vegetation Continuous Fields

287 product provides annual information about the percent tree cover, percent non-tree cover, and percent non-vegetated within
288 each 250-meter pixel globally (DiMiceli et al., 2015). Consequently, we compare vegetation cover proportions—sum of
289 percent tree cover and percent non-tree cover—to the sum of fractional PV and NPV. To align spatial and temporal
290 resolutions, we aggregated the sum of percent tree cover and percent non-tree cover to a 500-meter scale. Simultaneously,
291 we computed monthly fractional PV and NPV as annual averages. The GLASS fractional vegetation cover dataset, offering
292 an 8-day temporal frequency and dual spatial resolutions of 0.05° and 500 meters, was generated using a machine learning
293 approach correlating MODIS reflectance with fractional vegetation cover (Jia et al., 2015). In our study, the 500-meter
294 GLASS data was utilized to validate our estimated fractions. We computed annual averages from all the CLASS fractional
295 vegetation cover data within a year and compared it with the annual averages of Fractional PV and NPV. GEOV FCover
296 is a 10-day product estimated through the neural network using visible, near-infrared and shortwave infrared at 1km
297 resolution (Baret et al. 2013). We aggregate our product to a 1km spatial resolution, and compare their annual averages
298 with the annual averages of GEOV FCover.

299 Moreover, we also carry out a comparison with traditional linear spectral mixture analysis to demonstrate the advantages
300 of our spatio-temporally adaptive spectral mixture analysis. Such comparison is performed using average of monthly
301 $RMSE_{sma}$ of fully-constrained framework based on two fixed endmember spectral curves: (1) average of all spectral
302 spectra for each endmember and (2) existing spectral spectra from Small and Sousa (2019).

303 Furthermore, to validate the uncertainties of the hierarchical clustering, we select a spectral spectrum from selected
304 endmember spectra that exhibit the largest mean squared error from the mean of cluster for each cluster. These selected
305 spectral spectra were then used to reconstruct an extreme library of endmember spectra and used to estimate fractional
306 vegetation and soil using MESMA.

307 **2.5 Change of vegetation and soil fractions**

308 Mann-Kendall test is commonly referred to as a nonparametric test method, which is procedures that detects monotonic
309 trends of sequences over time (Kendall 1975; Mann 1945; Bradley 1968). When seasonal environmental data of interest
310 are available as time series for which the time intervals between adjacent observations are less than one year (i.e., daily,
311 weekly, and monthly sequences), a multivariate extension of the Mann-Kendall test has been advanced to handle seasonal
312 sequences. Besides, the seasonal Sen's slopes (change per unit of time) are commonly chosen to express this magnitude
313 (Hirsch et al. 1982; Sen and Kumar 1968). Therefore, we impose the seasonal Mann-Kendall test and seasonal Sen's method
314 to define trend and slope (annual change) of endmember fractions at the pixel level. The detailed information about
315 seasonal Mann-Kendall test and seasonal Sen's method can be found in Supplementary Methods. If the Mann-Kendall test

316 is not statistically significant ($p \geq 0.05$), we define net change as 0. If the trend test is significant ($p < 0.05$), we apply the
317 seasonal Sen's method to estimate the per-pixel net change between 2001 to 2022 (i.e., slope times 22 years). Besides, we
318 aggregate per-pixel net change of endmember fractions to spatial scales (such as country, biome, climate zone) to obtain
319 total area change estimates at these aggregated scales from 2001-2022 as,

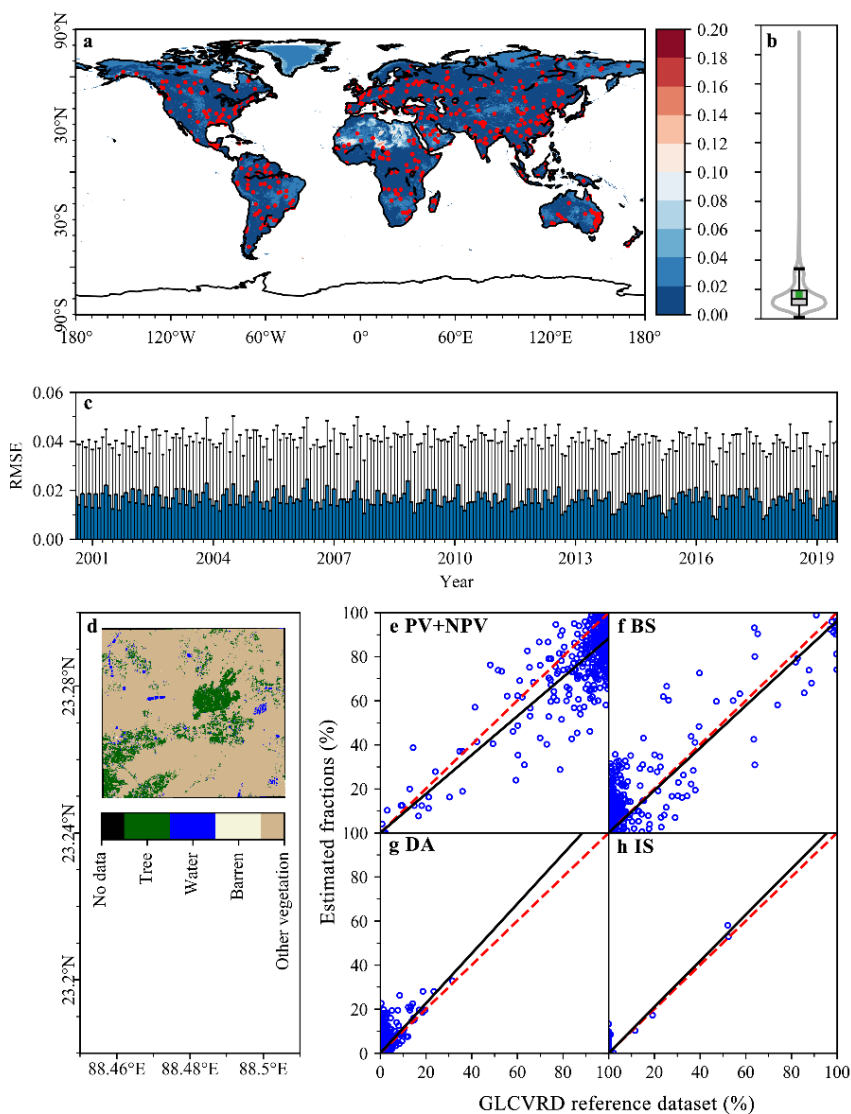
$$320 \quad \text{Net area change} = \sum_{i=1}^n T_i A_i N \quad (8)$$

321 Where T_i is Sen's slope of endmember fraction for a statistically significant pixel i , A_i represent area of pixel i , n is the
322 total number of such pixels in the region, N is the length of study period ($N = 22$).

323 **3 Results**

324 **3.1 Evaluation of monthly estimates of vegetation and soil fractions**

325 We utilize standard endmember spectra globally to estimate fractional vegetation-soil nexuses via MESMA. The simulated
326 results elucidate that the MESMA model performs well with an ideal model $RMSE_{sma}$ over globe (0.018 ± 0.022 , Fig. 3a-
327 c). We find the regions with $RMSE_{sma}$ above 0.02 account for less than one-fifth of the global area and are mainly
328 distributed in barren such as Sahara Desert and polar regions. This exceptional performance demonstrates the superiority
329 and low uncertainty of the model. This performance is also evidenced by evaluation results from GLCVRD (Fig. 3e-h,
330 Table S3). Specifically, the performance of PV+NPV, BS, and IS endmember estimates have MAE less than 0.118, RMSE
331 less than 0.149, R^2 greater than 0.592. Although the MAE (0.050) and RMSE (0.065) perform well, the R^2 of estimated
332 DA against measured DA presents only 0.156, largely attributed to the absence of estimations for shadows cast by smaller
333 vegetation within the validation dataset. In blocks with a DA greater than 0.2, the estimated DA and measured DA present
334 better consistency, in which the shadows of hills are well measured by GLCVRD. Moreover, we simultaneously select
335 another set of land cover reference data as validation samples (Fig.S5). The validation results demonstrate the superiority
336 of our estimation products, with MAE for PV, NPV, DA, BS, and IS abundances all less than 0.099, RMSE (Root Mean
337 Square Error) all less than 0.129, and R^2 all greater than 0.57. However, this set of validation data is also not ideal as it
338 fails to accurately estimate small-scale vegetation shadows and bare soil in highly vegetated area, resulting in a slight
339 overestimation of our DA and BS estimates near zero, accompanied by an underestimation of PV and NPV in high-value
340 areas.



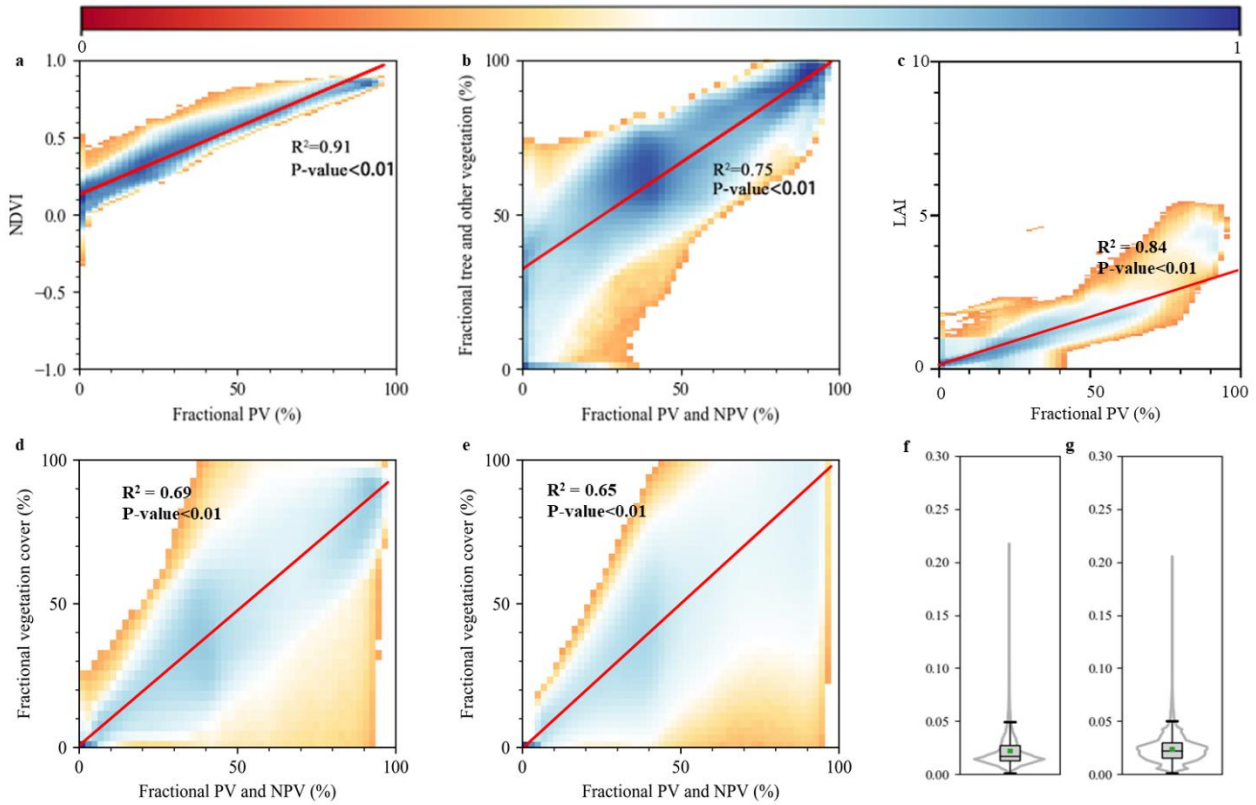
341

342 **Figure 3: Evaluation of global fractional endmember estimates.** a, the spatial pattern of average of monthly $RMSE_{sma}$
 343 from 2001 to 2022, the overlaid red dots were spatial distribution of the 5×5 km validation blocks of GLCVRD reference
 344 dataset ($n=500$). b, the boxplot and violin plot for average of monthly $RMSE_{sma}$ (a), which indicate mean $RMSE_{sma}$ over
 345 image is less than 0.02. c, monthly averaged $RMSE_{sma}$ from 2001 to 2022 with error bars. d, the schematic of detailed land
 346 cover classes of GLCVRD reference dataset. e-h, Scatter plots of PV+NPV, BS, DA, IS fractions against GLCVRD

347 reference dataset (tree + other vegetation, barren, water + shadow, ice & snow). Endmember fractions were derived from
348 corresponding year and month of each 5×5 km block achieved.

349 **3.2 Compared with other datasets and traditional spectral mixture analysis model.**

350 We compare our estimates vegetation and soil fractions dataset with NDVI, fractional PV and NPV against fractional tree
351 and non-tree vegetation of MOD44B vegetation continuous fields product and other fractional vegetation cover products.
352 We detected a strong positive relationship between PV fraction and NDVI. Yet, this correlation becomes less pronounced
353 when PV exceeds 50%, suggesting an evident saturation effect within NDVI (Fig. 4a). **This linear relationship also exists**
354 **in the relationship between PV and LAI, but a non-linear turning point occurs when PV exceeds 70% (Fig. 4c).** Furthermore,
355 PV and NPV fraction displays a significant positive association with the remaining three fractional vegetation cover
356 products (Fig. 4b, d, e). Specifically, the MOD44B vegetation continuous fields product reveals an R^2 of 0.75 with a p-
357 value below 0.01, the GLASS product displays an R^2 of 0.69 with a p-value below 0.01, and the GEOV Fcover product
358 exhibits an R^2 of 0.65, also with a p-value below 0.01. Nevertheless, within regions with lower vegetation cover, especially
359 drylands that present a higher presence of non-photosynthetic materials, current products (particularly GLASS and GEOV
360 Fcover) have not adequately evaluated vegetation coverage, resulting in some degree of underestimation in the outcomes
361 (Fig. 4c, d, Fig. S6a). Furthermore, we notice overestimation in the MOD44B vegetation continuous fields product in areas
362 where vegetation cover is less than 50%, mainly due to insufficient estimation of dark components (i.e., shadow of
363 vegetation and mountain, water) (Fig. 4b, Fig. S6c). In areas with denser vegetation cover, we found good alignment among
364 these products, especially with the MOD44B vegetation continuous fields product. However, the GLASS and GEOV
365 Fcover products tend to underestimate certain areas, primarily focusing more on green vegetation and overlooking non-
366 photosynthetic components (Fig. 4c, d, Fig. S6b). Moreover, both of two fully constrained linear spectral mixture models
367 are inferior to our framework since we consider the variability of the spectra in both time and space (Fig. 4e, f).



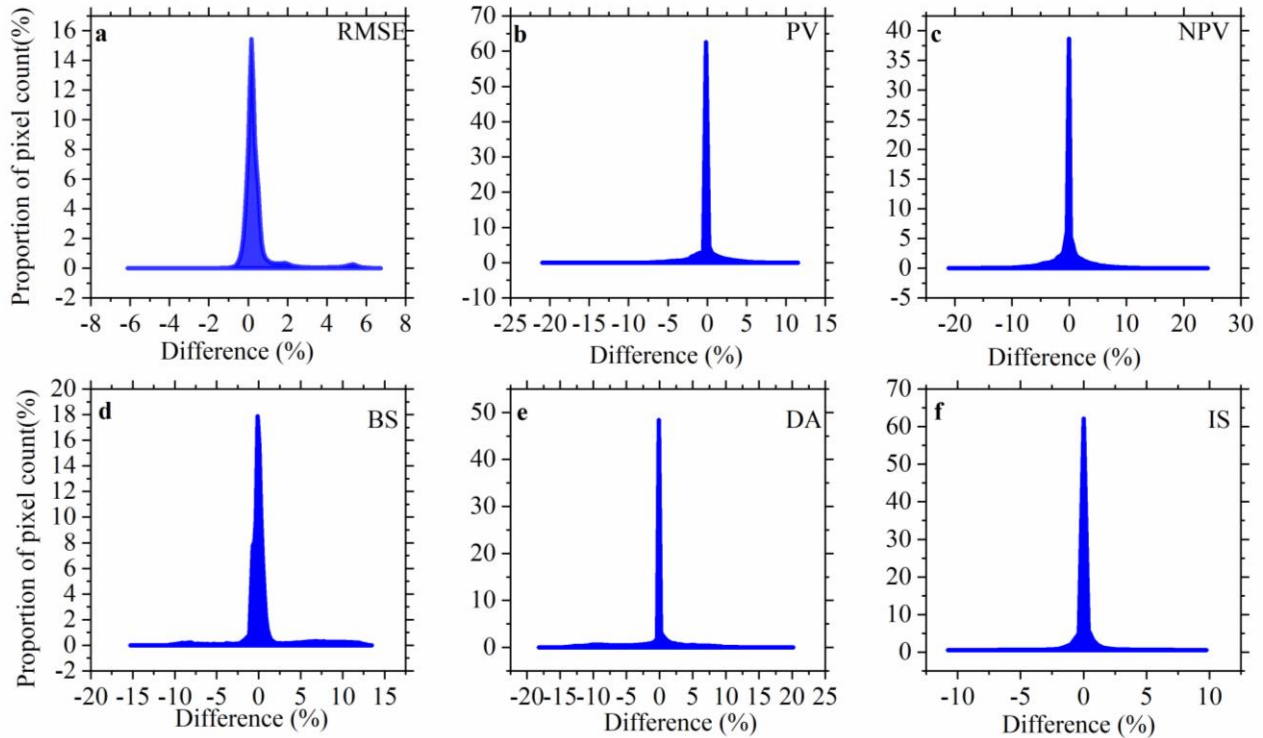
369

370 **Figure 4: Comparisons with other datasets and traditional spectral mixture analysis models.** a, b, c, d, e, the bi-
 371 dimensional histogram of fractional endmembers and other dataset with bin size of 2%, including fractional PV against
 372 NDVI (a), fractional PV and NPV against fractional tree and non-tree vegetation of MOD44B vegetation continuous fields
 373 product (b), fractional PV against LAI (c), fractional PV and NPV against GLASS fractional vegetation cover product (d),
 374 fractional PV and NPV against fractional vegetation cover of GEOV Fcover product (e); f, g, the boxplot and violin plot
 375 for average of monthly $RMSE_{sma}$ for two fixed endmember spectral curves using fully constrained linear spectral mixture
 376 models, including (e) average of all spectral spectra for each endmember and (f) existing spectral spectra from Small and
 377 Sousa (2019).

378 3.3 Uncertainties of estimates of global vegetation and soil fractions

379 It can be found that 90% of the $RMSE_{sma}$'s differences are concentrated within 1% (Fig. 5a), indicating the relative stability
 380 of the unmixed results from two libraries as well as the effectiveness of the clustering. These are also corroborated by the

381 differences between unmixed endmember fractions (Fig. 5b-e), as indicated by that more than 90% of global pixels have a
 382 difference of 10% or less, as well as more than 70% of global pixels present a difference up to 1%, except for the two
 383 endmembers with higher spatial variability (NPV, 61.59%; DA, 62.59%).

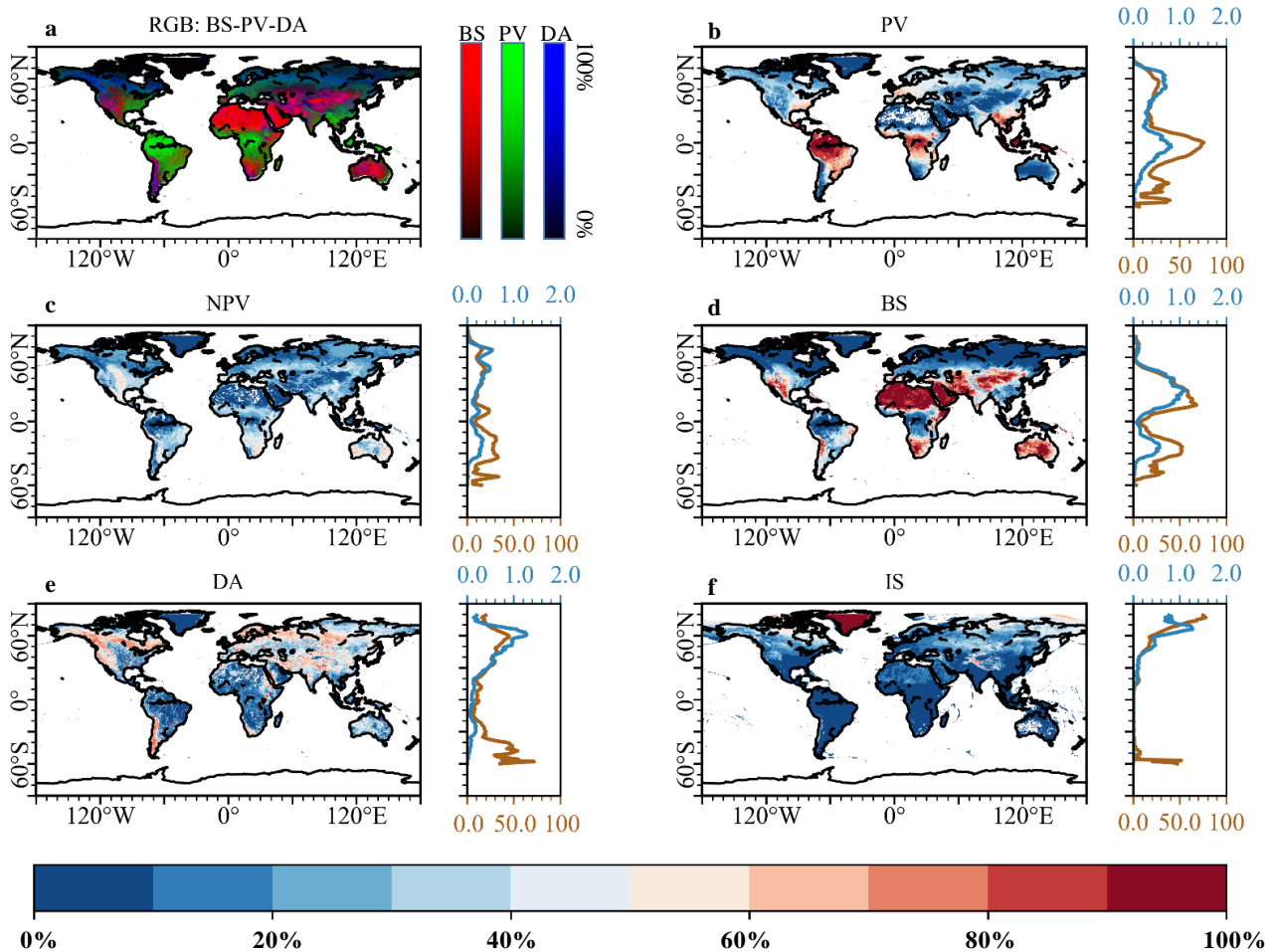


384
 385 **Figure 5: Difference in unmixed results between mean endmember library and endmember library in hierarchical**
 386 **cluster. a, b, c, d, e and f represent histogram of $RMSE_{sma}$, PV, NPV, BS, DA and IS.**

387 3.4 Spatial distribution of global vegetation and soil fractions

388 Globally averaged monthly gradations of five surface vegetation and soil components are illustrated in Fig. 6. Our estimates
 389 depict that PV cover presents the largest area for both 30°-60°N and 0-30°S, which together account for more than half of
 390 the total global terrestrial vegetation area. We find the average PV fraction in the Northern Hemisphere is significantly less
 391 than that in the Southern Hemisphere, especially in the Amazon, although the area of PV at 30°-60°N is slightly greater
 392 than that of 0-30°S. Dominated by foliage-free desert vegetation and agricultural straw, NPV is mainly found in the semi-
 393 arid regions (e, g., USA, western China, and Australia) and croplands. BS is also located in the drylands of the Sahara,
 394 western Asia, and west-central Australia in terms of both fraction and total area. DA and IS, on the one hand, are mainly

395 concentrated in terrestrial water bodies and mountains, Greenland and global high mountains of the Himalayas and the
 396 Andes, respectively.



397

398 **Figure 6: Global average of monthly fractional endmembers from 2001 to 2022.** a, Spatialized RGB composition of
 399 three averages of monthly fractional endmembers (RGB: BS-PV-DA). b-f, average of PV, NPV, BS, DA, and IS fractions.
 400 Shaded subplots are average of fractional endmembers (% , orange, lower) and area of endmembers (fraction × pixel
 401 area, ×10⁶ km², blue, upper) at respective latitudes, taking each degree as the statistical standard.

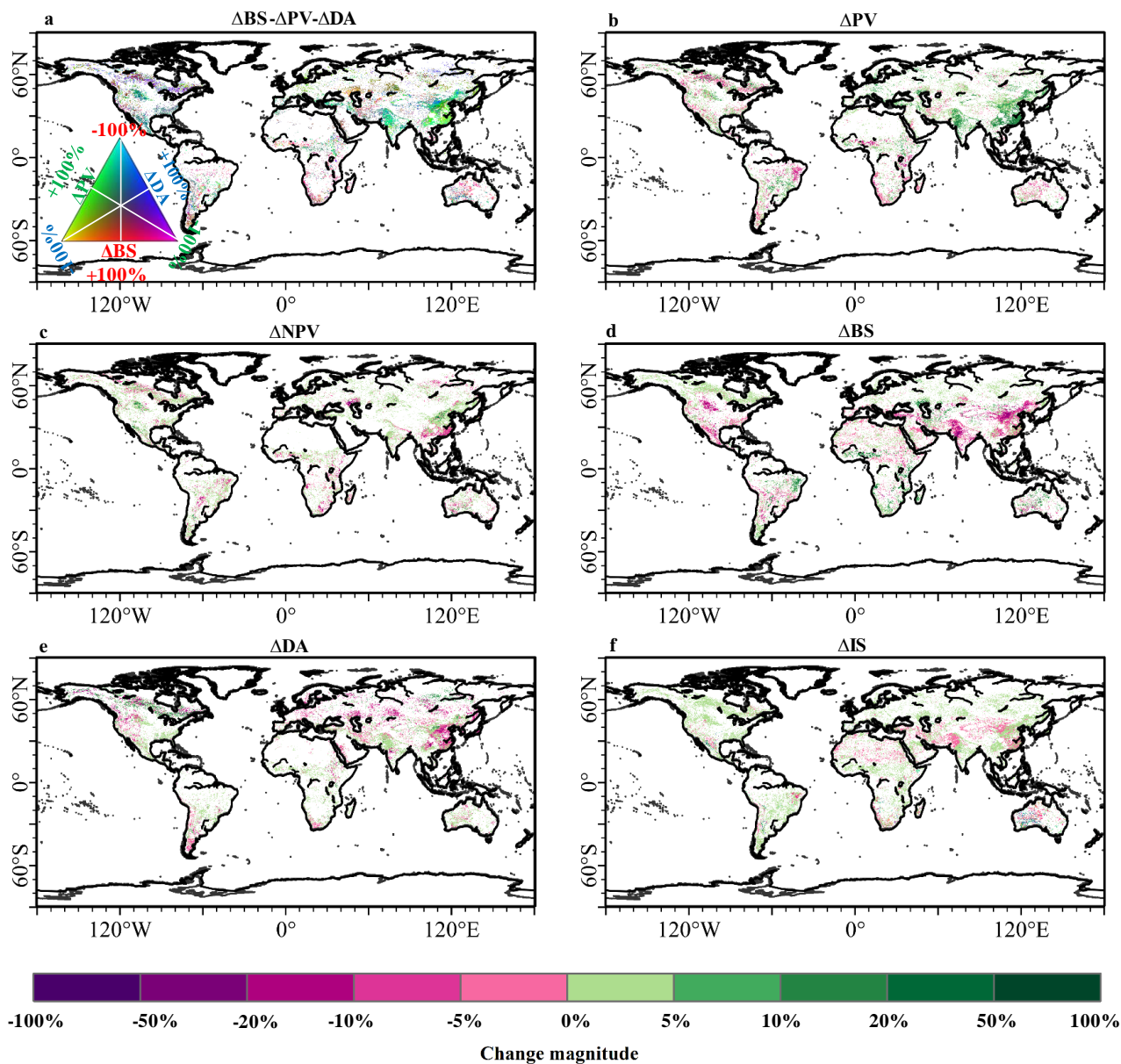
402 **3.5 Globally and regionally fractional endmembers dynamics**

403 The total area of PV increases $9.35 \times 10^5 \text{ km}^2$ from 2001 to 2022, which represents a +1.88% change relative to 2001 green
404 vegetation (Fig. 7; Table S4). This increased trend results from higher magnitude of gain ($1.57 \times 10^6 \text{ km}^2$), nearly 2.5 times
405 the loss area. Our PV area gain estimate basically agrees in magnitude with the global vegetation continuous fields
406 product's estimate of net vegetation area change ($1.36 \times 10^6 \text{ km}^2$), despite differences in the time period covered (1982-
407 2016) and definition (tree and other vegetation) (Song et al. 2018). Temperate, arid and cold regions together contribute
408 more than 90% of the greening area (Fig. 8; Table S4). In these areas, the China and India are two major contributors (Fig.
409 S7) through land use management like ecological afforestation and agricultural expansion (Chen et al. 2019). Within
410 Brazilian Amazon, we find a large area of PV loss (Fig. S7), which is also supported estimates of forest cover and loss
411 (Qin et al. 2019).

412 A decreasing trend is observed in NPV globally ($2.19 \times 10^5 \text{ km}^2$), representing a -1.45% change relative to 2001 NPV area
413 (Fig. 7; Table S4). Tropical and temperate regions together contribute more than 80% of the loss area of NPV, which may
414 result from global warming induced tree greening. Although the arid is major source of NPV ($2.75 \times 10^6 \text{ km}^2$ in 2001, 18.2%
415 of globe NPV area), the change area of NPV is only less than 10000 km^2 (Fig. 8; Table S4).

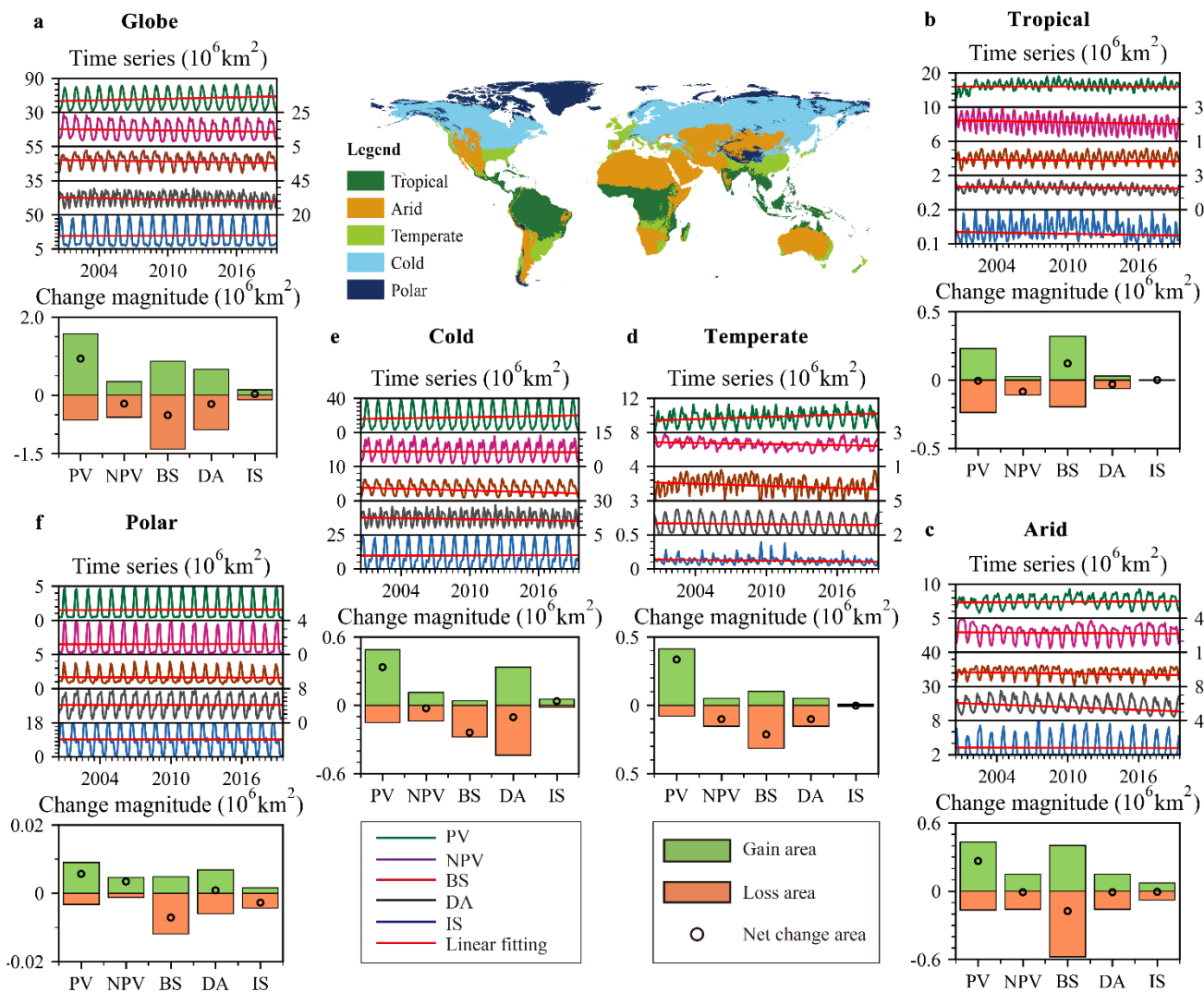
416 In the context of the greening of the vegetation, the degree of BS is reduced by $5.14 \times 10^5 \text{ km}^2$ during study period, indicating
417 a -1.09% change relative to initial BS of 2001. The decreased global BS trend occurs in temperate, arid and cold regions,
418 accounting over 90% of net BS change area. In contrast, tropical region appears an increasing trend ($+1.22 \times 10^5 \text{ km}^2$), and
419 thus offset the decline in BS in the rest of the regions (Fig. 8; Table S4). This outcome results from the forest loss induced
420 soil exposure in Brazilian Amazon and Southeast Asia (Fig. S7). Meanwhile, the total area of DA also represents a net
421 change of $-2.27 \times 10^5 \text{ km}^2$, from 2001 to 2022, which represents a -0.69% change relative to 2001 DA area. The largest
422 negative contributions to the decreased global DA appear in cold (46.26%) and arid (32.87%) (Fig. 6; Table S4). We
423 observed an increase of $2.46 \times 10^4 \text{ km}^2$ in IS globally, which represents a +0.11% change relative to 2001 IS. Such positive
424 trend is mainly benefited by the increase of snow and ice in the cold regions, in which the net increase area is 1.5 times

425 greater than the global net IS change (Fig. 8; Table S4). This is caused by the increase of snowfall. However, global
 426 warming is causing a substantial melting of snow and ice, resulting in the arid, tropical, temperate and polar regions show
 427 a decreasing trend in IS cover.



428

429 **Figure 7: Globally fractional endmembers dynamics at pixel level.** a, composited RGB image with Δ BS, Δ PV, and
 430 Δ DA. b-f, the change magnitude (%) in each pixel for estimated endmembers, i.e., Δ PV, Δ NPV, Δ BS, Δ DA, and Δ IS.
 431 Pixels showing a statistically significant trend (Seasonal Mann–Kendall test, $P < 0.05$) for either endmember are depicted
 432 on the change map.



433

434 **Figure 8: Global and regional fractional endmembers dynamics.** The middle subgraph is aggregated five Köppen-Geiger
435 climate classes. **a-f**, the gain area, loss area and net change area for five land surface endmembers in globe (**a**) and five
436 climate zones, i.e., tropical (**b**), arid (**c**), temperate (**d**), cold (**e**), and polar (**f**).

437 **4 Discussions**

438 **4.1 Advances and limitations of estimates of global vegetation and soil fractions**

439 This paper implements a globally monthly estimates of fractional vegetation-soil nexuses in 2001–2022 via high-accuracy
440 and time-consuming MESMA algorithm at sub-pixel scale (Roberts et al. 1998), benefited from the GEE platform that can
441 provide powerful computational processing to realize planetary-scale analysis of geospatial data. We can more
442 conveniently target the most optimal model from 692 combination models for each MODIS pixel (500 m), thus help to
443 understand the specific vegetation-soil compositional structures in each pixel or region. Such scheme can improve the
444 ecologists and managers understanding of multifaceted terrestrial ecosystems for differentiated measures. Moreover, these
445 fractional endmembers have been proven their potential for application in land use cover classification (Sun et al., 2020),
446 time-series evolutionary pathways (Sun et al., 2021; Daldegan et al., 2018) and biophysical process modelling (Sun et al.,
447 2022; Sousa and Small, 2018). This globally comprehensive record of monthly vegetation and soil fractions during the
448 period 2001–2022 may provide basic data for quantification and modelling of global change, as well as provide an
449 important foundation for measuring sustainable development goals such as land degradation neutrality (Chasek et al., 2019;
450 Sun et al., 2019).

451 Our product can overcome the problem of saturation of NDVI in the regions embodying high coverage vegetation. Such
452 advance can be supported by previous regional comparison research (Rogan et al. 2002; Sun et al. 2019; Sun et al. 2020).
453 Additionally, the diversity of information stands as one of the strengths of this dataset, encompassing the five primary
454 components of the Earth's land surface globally. Moreover, it can be extended to encompass more types through different
455 levels of clustering. For instance, the DA component has not been emphasized in many datasets, yet current scientific
456 research underscores the need for increased attention to vegetation shadows (Zeng et al., 2023). Although our DA
457 component represents various types across different land regions, such as water bodies, shadows, bare rocks, this dataset
458 may effectively enhance our precise understanding of complex vegetation structures. **The NPV component is a vital
459 element in arid ecosystems and represents a crucial part of vegetation biomass. Our dataset, by finely characterizing NPV,
460 not only aids in understanding the evolving features of vegetation structure under photosynthetic and non-photosynthetic
461 interactions (Guerschman et al. 2015), but also contributes to a more accurate quantification of global biomass in arid land
462 systems (Smith et al. 2019).**

463 Moreover, our product demonstrates good scalability in terms of time and endmember types. These monthly estimates of
464 fractional vegetation-soil nexuses can be upgraded to multi-timescale (daily, yearly) products to serve different needs, and
465 thus provide time series of multicomponent information on surface heterogeneous composition and interactive evolution.
466 Besides, considering the meaningful physical interpretations of endmember fraction values, these endmembers can be
467 conveniently integrated across different temporal and spatial scales using spatiotemporal fusion methods (Zhang et al.
468 2018). The temporal and spatial variability of endmembers has always been a significant constraint in obtaining global-
469 scale vegetation and soil fractions from imagery (Wang et al. 2021). The spatio-temporally adaptive framework employed
470 helps to increase the representativeness of endmember selection, and MESMA also considers the suitability of each
471 combination of these endmembers within each pixel. However, considering the limitations of computational resources, our
472 solution on hierarchical clusters of the endmember spectra can improve considerably cost-effective unmixing of long time-
473 series satellite records over globe under the trade-offs of certain accuracy requirements (Fig. 3). With the assumption of
474 increased computational power in the future, we believe that utilization of combination models from selected endmember
475 spectra (35 GV spectra, 40 BS spectra, 25 NPV spectra, 16 DA spectra, and 15 IS spectra) or expanded endmember spectra
476 may further improve the accuracy and stability of estimates of gradations of five surface vegetation and soil components
477 at global scale.

478 However, due to the absence of corresponding reference data for validation, we solely rely on two high-quality land cover
479 reference datasets for validation. Unfortunately, these datasets do not intricately characterize small-scale shadows and bare
480 soil within complex vegetation structures. Consequently, this leads to a misconception in the validation, where our DA and
481 BS are overestimated in low-value areas and vegetation is underestimated in high-value areas (Fig. 3, Fig.S5). Therefore,
482 in the future, there is a need to further develop high-quality relevant reference data. Considering that MOD44B vegetation
483 continuous fields product provides a gradation of three surface cover components: percent tree cover, percent non-tree
484 cover, and percent bare, the dark components (i.e., shadow of vegetation and mountain, water) are not quantified. Therefore,
485 fractional PV and NPV is overall biased high, especially in areas with PV and NPV less than 0.50 (Fig. 4b; Fig. S6b).
486 Besides, we also observed a certain degree of underestimation in these three datasets in regions with lower vegetation cover
487 compared to our data. This is mainly because these datasets focus solely on green vegetation, especially GLASS and GEOV
488 Fcover (Baret et al. 2013; Jia et al., 2015), and do not accurately estimate non-photosynthetic vegetation in arid regions.
489 The above comparisons demonstrate our precision advantage in fine extraction of multiple endmembers. **Given the
490 importance of NPV in ecological research, undertaking separate validation and comparisons between PV and NPV
491 represents a critical foundational effort. While detailed maps of a representative region illustrate the reliability and
492 advantages of our NPV estimation over other products (Fig. S6), the current lack of equivalent products highlights the need
493 for ongoing development. Enhancing quantitative comparison efforts will be essential to bolster the feasibility, accuracy**

494 **and validity of our NPV product in future studies.** We observed higher $RMSE_{sma}$ values in seemingly homogeneous areas
495 like the Sahara Desert and Arctic regions. However, within these regions, there often exist extremely diverse land cover
496 types, such as high and low reflectance sands and ice. When selecting endmembers and hierarchical clustering models, we
497 might not have adequately considered these extreme spectral curves. As a result, these extreme areas exhibit a higher
498 uncertainty.

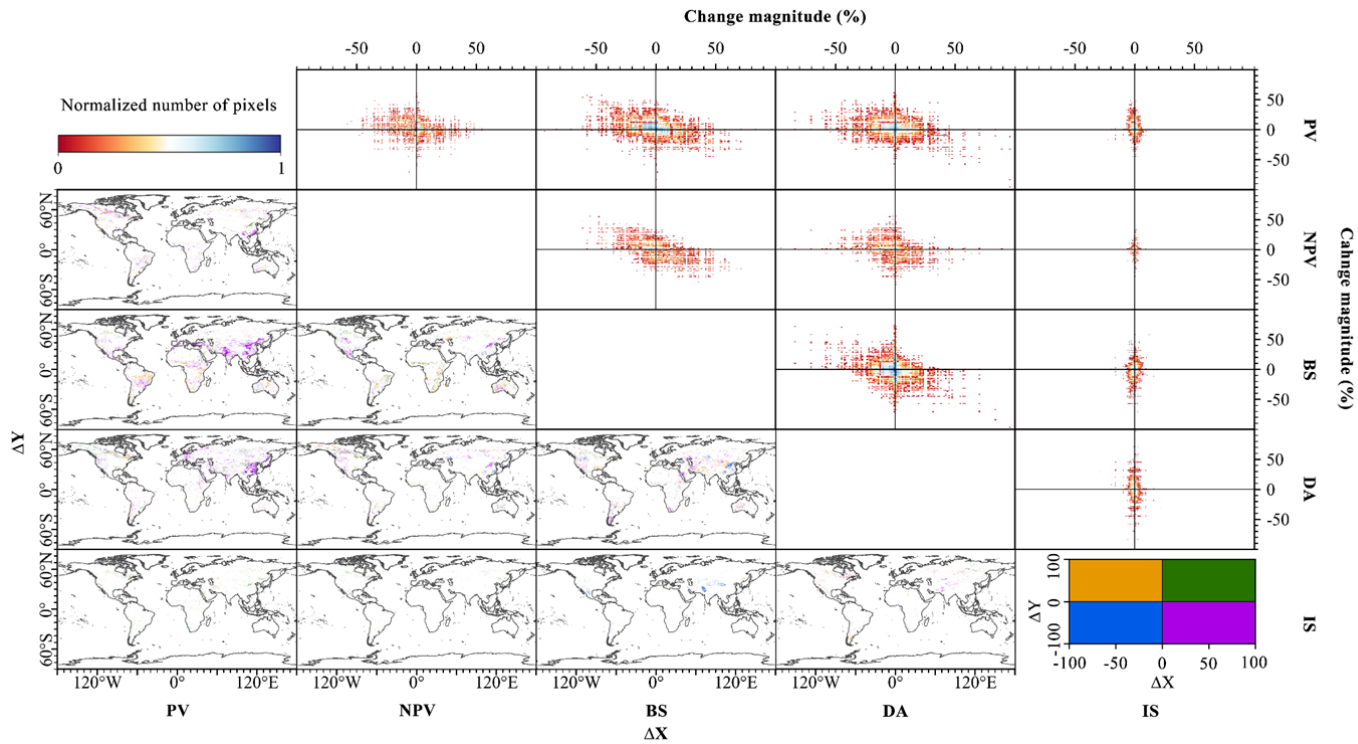
499 **4.2 Implications of global and regional shifts from pairs of two endmembers**

500 We find greening of Earth characterized by increased photosynthetic vegetation and reduced bare soil exposure, is observed
501 in temperate and cold countries such as Russia (Fig. 9; Figure S3). This finding is in agreement with the finding of climate-
502 driven greening trend in Northern Hemisphere (Piao et al. 2006). While the biomass decreases, exhibited as decreased PV
503 and increased BS (Fig. 9), presented only half of the global climate-driven greening. These findings imply a global trend
504 towards greening in the context of global warming, as supported by a large number of published studies on global
505 vegetation change (Chen et al. 2019; Piao et al. 2006; Song et al. 2018). Moreover, the polar zone is hotspot of ice melting
506 and agrees an accepted fact of accelerated retreat of glaciers and ice under global warming (Hugonnet et al. 2021; Zemp et
507 al. 2019).

508 Besides, the overexploitation of resources is one of environmental problems of interest and an important factor in causing
509 above climate change and disasters. Global overexploitation has led to problems such as vegetation degradation and
510 intensive utilization of agricultural land. The human overexploitation of forest and grassland induced biomass decrease
511 present a decrease of PV and increase of BS (Fig. 9; Fig. S7), especially over tropical rainforest of Brazilian Amazon and
512 South Asian. This finding agrees with deforestation and agriculturalization in these regions provided by previous studies
513 (Qin et al. 2019; Zeng et al. 2018). Within agricultural area, the agricultural intensification is a human-driven greening
514 process characterized by increased photosynthetic vegetation and reduced bare soil, this shift mainly occurs in India and
515 the North and Northeast China Plain (Fig. 9; Fig. S7) (Chen et al., 2019). We also found urbanization-driven biomass
516 decrease in the global terrestrial ecosystems, especially in China and North America (Fig. 9; Fig. S7), resulted from
517 occupation of agricultural and ecological lands during urban sprawl (Kuang et al., 2020, 2021; Zhao et al., 2022).

518 Eco-restoration depicts a process that currently needs urgent attention in our understanding and utilization of resources and
519 environment. Different from climate-driven greening that presents trends of increasing PV and decreasing BS, the human-
520 driven afforestation shows positive trends of both PV and NPV, mainly attributed to recent implementing of policies on
521 the ecological restoration through large number of protective forests planted (Fig. 9; Fig. S7). These afforested regions are
522 primarily found over China, Europe, North America, supported by previous study on greening world (Chen et al. 2019).

523 Moreover, Green space construction in urbanized regions has been carried out, integrated with road construction and city
524 renovation, and generate an increasing of footprint of urban greening, especially in China (Fig. 9; Fig. S7).
525 This dataset can serve as a baseline for enhancing our comprehension of heterogeneous surface dynamics and modeling
526 Earth's biophysical processes through a multi-endmember coupling perspective, may significantly advance future research
527 by serving as a foundational reference for delving deeper into complex land systems. Anticipating its potential applications
528 across diverse domains such as ecology, climate studies, and urban planning, this dataset emerges as a pivotal resource. Its
529 multifaceted utility is expected to play a pivotal role in informing environmental management decisions, advancing studies
530 on ecological shifts, predicting climate trends, and facilitating strategic landscape planning.



531

532 **Figure 9: Characteristics of each pair of two endmembers.** The bottom left corner was global maps of co-location of paired two endmembers.
 533 Pixels showing a statistically significant trend (Seasonal Mann–Kendall test, $P < 0.05$) in both endmembers are depicted on the map.
 534 The color of each pixel was displayed in quadrant of ΔX and ΔY , where ΔX and ΔY are horizontal and vertical endmembers, respectively. The top right corner
 535 was 2D histogram of change magnitude (%) of paired two endmembers. the x-axes and y-axes were represented by ΔX and ΔY , respectively. These
 536 2D histogram plots were created with bin size of 1% for both axes. The colour bar was normalized number of pixels in each bin on a log scale.

5 Data availability

The data about fractional five surface vegetation and soil components can be exported from GEE platform via provided codes or are available on Science Data Bank (<https://doi.org/10.57760/sciencedb.13287>, Sun and Sun, 2023). The first dataset includes five fractions from 2001-2011, another includes five fractions from 2012-2022. The file is a compressed month-by-month GeoTIFF data for each year, according to the grid of longitude 60° and Latitude 50°. Since the dataset for each year includes 216 files, named as “SMA_year_(month-1)_gridid.tif”, like “SMA_2001_0_0.tif”. The public datasets have been listed in the Methods.

6 Code availability

The GEE codes for the MESMA and seasonal Mann-Kendall test will be available at GitHub (https://github.com/qiangsunpingzh/GEE_mesma) or other platforms upon publication; Common code for generating figures is available at <https://matplotlib.org/>.

7 Conclusions

In this paper, to provide locally detailed socio-ecological knowledge about globally multifaceted changes in fractional vegetation-soil nexuses under climate change and anthropogenic impacts, we estimated monthly vegetation and soil fractions in 2001–2022 that provide multi-component information on surface heterogeneous composition based on a spatio-temporally adaptive spectral mixture analysis framework. This product of monthly vegetation and soil fractions from 692 combination models can provide an accurate estimate of surface heterogeneous composition, better than previous vegetation index and vegetation continuous fields product, as well as traditional fully constrained linear spectral mixture models. This solution can both improve considerably cost-effective unmixing of long time-series satellite records over globe and meet the accuracy requirements. Based on these estimates of vegetation and soil fractions, we find a greening trend of Earth, as indicated by an increase of the total area of PV, which represents a +1.88% change relative to 2001 green vegetation. This greening trend can be found all climatic zones other than the tropics. In addition to the trends in the greening reported by other study, we also found that the increase in PV was accompanied by a decreasing trend in BS, DA and NPV in most regions. And there is a trend of simultaneous increase in PV and NPV in central and southwest China during afforestation activities. Therefore, a combination between interactive changes of vegetation and soil fractions can be adopted as a valuable measurement of climate change and anthropogenic impacts.

Author contributions

Q.S., D.S., P.Z., and H.L. designed the study. Q.S. and P.Z. performed the analysis with support from D.S., H.L., J.H., S.L.,
565 and S.Y. Q.S., P.Z., and D.S. drafted the paper. Q.S., P.Z., X.J., M.S., F.L., W.D., S.M., A.L., Y.Z., and H.L. collected data
and prepared figures. All authors contributed to interpretation of the results and discussions as well as manuscript editing.

Competing interests

The contact author has declared that none of the authors has any competing interests.

Acknowledgements

570 We thank Bruce W. Pengra for providing the GLCVRD reference dataset.

Financial support

Funding for this work was provided by National Key R&D Program of China (grant no. 2023YFB3907604) and the National
Natural Science Foundation of China (grant nos. 42001234, 42071252).

References

- 575 Alkama, R., Cescatti, A.: Biophysical climate impacts of recent changes in global forest cover. *Science*, 351, 600-604,
<https://doi.org/10.1126/science.aac8083>, 2022.
- Baumann, M., Levers, C., Macchi, L., Bluhm, H., Waske, B., Gasparri, N.I., Kuemmerle, T.: Mapping continuous fields of
tree and shrub cover across the Gran Chaco using Landsat 8 and Sentinel-1 data. *Remote Sens. Environ.*, 216, 201-211,
<https://doi.org/10.1016/j.rse.2018.06.044>, 2018.
- 580 Beck, H. E., Zimmermann, N. E., McVicar, T. R., Vergopolan, N., and Wood, E. F.: Present and future kppen-geiger climate
classification maps at 1-km resolution. *Scientific Data*, 5, 180214. <https://doi.org/10.1038/sdata.2018.214>, 2018.
- Baret, F., Weiss, M., Lacaze, R., Camacho, F., Makhmara, H., Pacholczyk, P., Smets, B.: GEOV1: LAI, FAPAR Essential
Climate Variables and FCover global times series capitalizing over existing products. Part1: Principles of development and
production. *Remote Sens. Environ.*, 137, 299–309, <https://doi.org/10.1016/j.rse.2013.02.030>, 2013
- 585 Boardman, J.W.: Automating spectral unmixing of aviris data using convex geometry concepts. In, *Jpl Airborne Geoscience
Workshop*. 2013.
- Bradley, J.V.: *Distribution-Free Statistical Test*. Englewood Cliffs: Prentice-Hall, 1968.

- Chasek, P., Mariam, A.S., Orr, B. J., Luise, A., Ratsimba, H. R., Safriel, U.: Land degradation neutrality: the science-policy interface from the UNCCD to national implementation. *Environmental science & policy*, 92, 182-190, 590 <https://doi.org/10.1016/j.envsci.2018.11.017>, 2018.
- Chen, C., Park, T., Wang, X., Piao, S., Xu, B., Chaturvedi, R.K., Fuchs, R., Brovkin, V., Ciais, P., Fensholt, R.: China and India lead in greening of the world through land-use management. *Nature Sustainability*, 2, 122-129, <https://doi.org/10.1038/s41893-019-0220-7>, 2019
- Daldegan, G.A., Roberts, D.A., Ribeiro, F.: Spectral mixture analysis in Google Earth Engine to model and delineate fire scars 595 over a large extent and a long time-series in a rainforest-savanna transition zone. *Remote Sens. Environ.*, 232, 111340. <https://doi.org/10.1016/j.rse.2019.111340>, 2019
- DiMiceli, C., Carroll, M., Sohlberg, R., Kim, D., Kelly, M., Townshend, J.: MOD44B MODIS/Terra Vegetation Continuous Fields Yearly L3 Global 250m SIN Grid V006. In: NASA EOSDIS Land Processes DAAC, 2015.
- Elmore, A.J., Mustard, J.F., Manning, S.J., Lobell, D.B.: Quantifying vegetation change in semiarid environments: Precision 600 and accuracy of spectral mixture analysis and the normalized difference vegetation index. *Remote Sens. Environ.*, 73, 87-102, [https://doi.org/10.1016/S0034-4257\(00\)00100-0](https://doi.org/10.1016/S0034-4257(00)00100-0), 2000
- Franke, J., Roberts, D.A., Halligan, K., Menz, G.: Hierarchical Multiple Endmember Spectral Mixture Analysis (MESMA) of hyperspectral imagery for urban environments. *Remote Sens. Environ.*, 113, 1712-1723, <https://doi.org/10.1016/j.rse.2009.03.018>, 2022.
- 605 Friedl, M. and Sulla-Menashe, D. MCD12Q1 MODIS/Terra+Aqua Land Cover Type Yearly L3 Global 500m SIN Grid V006.: NASA EOSDIS Land Processes DAAC, 2015.
- Fritz, S., See, L., Perger, C., McCallum, I., Schill, C., Schepaschenko, D., Duerauer, M., Karner, M., Dresel, C., Laso-Bayas, J. C., Lesiv, M., Moorthy, I., Salk, C. F., Danylo, O., Sturn, T., Albrecht, F., You, L., Kraxner F., Obersteiner, M.: A global dataset of crowdsourced land cover and land use reference data. *Scientific data*, 4, 1-8, <https://doi.org/10.1038/sdata.2017.75>, 610 2017.
- Guerschman, J. P., Hill, M. J., Renzullo, L. J., Barrett, D. J., Marks, A. S., Botha, E. J.: Estimating fractional cover of photosynthetic vegetation, non-photosynthetic vegetation and bare soil in the Australian tropical savanna region upscaling the EO-1 Hyperion and MODIS sensors. *Remote Sens. Environ.*, 113(5), 928-945, <https://doi.org/10.1016/j.rse.2009.01.006>, 2009.
- Guerschman, J. P., Scarth, P. F., McVicar, T. R., Renzullo, L. J., Malthus, T. J., Stewart, J. B., Trevithick, R.: Assessing the 615 effects of site heterogeneity and soil properties when unmixing photosynthetic vegetation, non-photosynthetic vegetation and bare soil fractions from Landsat and MODIS data. *Remote Sens. Environ.*, 161, 12-26, <https://doi.org/10.1016/j.rse.2015.01.021>, 2015

- Heinz, D.C., Chein-I-Chang: Fully constrained least squares linear spectral mixture analysis method for material quantification in hyperspectral imagery. *IEEE Transactions on Geoscience & Remote Sensing*, 39, 529-545, 2002. <https://doi.org/10.1109/36.911111>, 2002.
- Hirsch, R.M., Slack, J.R., Smith, R.A.: Techniques of trend analysis for monthly water quality data. *Water Resour. Res.*, 18, 107-121, <https://doi.org/10.1029/WR018i001p00107>, 1982.
- Hugonnet, R., McNabb, R., Berthier, E., Menounos, B., Kienast, A.: Accelerated global glacier mass loss in the early twenty-first century. *Nature*, 592, 726-731, <https://doi.org/10.1038/s41586-021-03436-z>, 2021.
- IPCC: Climate Change 2013: The Physical Science Basis. 2013
- Jia K, Liang S, Liu S, Li Y, Xiao Z, Yao Y, Jiang B, Zhao X, Wang X, Xu S.: Global land surface fractional vegetation cover estimation using general regression neural networks from MODIS surface reflectance. *IEEE Trans Geosci Remote Sens.*, 53,4787–4796, <https://doi.org/10.1109/TGRS.2015.2409563>, 2015.
- Kendall, M.G. 1975. Rank correlation methods. London: Charles Griffin
- Kuang, W., Du, G., Lu, D., Dou, Y., Miao, C.: Global observation of urban expansion and land-cover dynamics using satellite big-data. *Sci Bull*, 66, 297-300, <https://doi.org/10.1016/j.scib.2020.10.022>, 2020.
- Kuang, W., Zhang, S., Li, X., Lu, D.: A 30 m resolution dataset of china's urban impervious surface area and green space, 2000-2018. *Earth System Science Data*, 13. 63–82, <https://doi.org/10.5194/essd-13-63-2021>, 2021.
- Lawrence, D., Vandecar, K.: Effects of tropical deforestation on climate and agriculture. *Nat Clim Change*, 5, 27-36, <https://doi.org/10.1038/nclimate2430>, 2015.
- Lewińska, K. E., Hostert, P., Buchner, J., Bleyhl, B., Radeloff, V. C.: Short-term vegetation loss versus decadal degradation of grasslands in the Caucasus based on Cumulative Endmember Fractions. *Remote Sens. Environ.*, 248, 111969. <https://doi.org/10.1016/j.rse.2020.111969>, 2020.
- Liu, H., Gong, P., Wang, J., Clinton, N., Bai, Y., and Liang, S.: Annual dynamics of global land cover and its long-term changes from 1982 to 2015, *Earth Syst. Sci. Data*, 12, 1217–1243, <https://doi.org/10.5194/essd-12-1217-2020>, 2020.
- Liu, X., Huang, Y., Xu, X., Li, X., Zeng, Z.: High-spatiotemporal-resolution mapping of global urban change from 1985 to 2015. *Nature Sustainability*, 564-570, <https://doi.org/10.1038/s41893-020-0521-x>, 2020.
- James, G., Witten, D., Hastie, T., & Tibshirani, R.: An introduction to statistical learning. New York: springer, <https://doi.org/10.1007/978-1-0716-1418-1>. 2013
- Mann, H.B.: Nonparametric tests against trend. *Econometrica: Journal of the econometric society*, 245-259, <https://doi.org/10.2307/1907187>, 1945.

- Meyer, T., Okin, G.S.: Evaluation of spectral unmixing techniques using MODIS in a structurally complex savanna environment for retrieval of green vegetation, nonphotosynthetic vegetation, and soil fractional cover. *Remote Sens. Environ.*, 161, 122-130, <https://doi.org/10.1016/j.rse.2015.02.013>, 2015.
- 650 Mu, X. H., Liu, Q. H., Ruan, G. Y., Zhao, J., Zhong, B., Wu, S. L., and Peng. J. J.: A 1 km/5 day Fractional Vegetation Cover Dataset Over China-ASEAN (2013). *Journal of Global Change Data & Discovery* 1. 45–51. <https://doi.org/10.3974/geodp.2017.01.07>. 2017
- Okin, G.S.: Relative spectral mixture analysis — A multitemporal index of total vegetation cover. *Remote Sens. Environ.*, 106, 467-479, <https://doi.org/10.1016/j.rse.2006.09.018>, 2007.
- 655 Okin, G.S., Clarke, K.D., Lewis, M.M.: Comparison of methods for estimation of absolute vegetation and soil fractional cover using MODIS normalized BRDF-adjusted reflectance data. *Remote Sens. Environ.*, 130, 266-279, <https://doi.org/10.1016/j.rse.2012.11.021>, 2013
- Olofsson, P., Stehman, S.V., Woodcock, C.E., Sulla-Menashe, D., Sibley, A.M., Newell, J.D., Friedl, M.A., Herold, M.: A global land-cover validation data set, part I: Fundamental design principles. *Int. J. Remote Sens.*, 33, 5768-5788, 660 <https://doi.org/10.1080/01431161.2012.674230>, 2012.
- Pengra, B., Long, J., Dahal, D., Stehman, S.V., Loveland, T.R.: A global reference database from very high resolution commercial satellite data and methodology for application to Landsat derived 30 m continuous field tree cover data. *Remote Sens. Environ.*, 165, 234-248, <https://doi.org/10.1016/j.rse.2015.01.018>, 2015
- Piao, S., Friedlingstein, P., Ciais, P., Zhou, L., Chen, A.: Effect of climate and CO₂ changes on the greening of the Northern Hemisphere over the past two decades. *Geophys. Res. Lett.*, 33, L23402, <https://doi.org/10.1029/2006GL028205>, 2006. 665
- Qin, Y., Xiao, X., Dong, J., Zhang, Y., Wu, X., Shimabukuro, Y., Arai, E., Biradar, C., Wang, J., Zou, Z.: Improved estimates of forest cover and loss in the Brazilian Amazon in 2000–2017. *Nature Sustainability*, 2, 764-772, <https://doi.org/10.1038/s41893-019-0336-9>, 2019.
- Qin, Y., Xiao, X., Wigneron, J., Ciais, P., Brandt, M., Fan, L., Li, X., Crowell, S., Wu, X., Doughty, R.: Carbon loss from forest degradation exceeds that from deforestation in the Brazilian Amazon. *Nat Clim Change*, 11, 442-448, 670 <https://doi.org/10.1038/s41558-021-01026-5>, 2021.
- Rashed, T., Weeks, J.R., Roberts, D., Rogan, J., Powell, R.: Measuring the physical composition of urban morphology using multiple endmember spectral mixture models. *Photogrammetric Engineering & Remote Sensing*, 69, 1011-1020, <https://doi.org/10.14358/PERS.69.9.1011>, 2003

- 675 Réjou-Méchain, M., Mortier, F., Bastin, J., Cornu, G., Barbier, N., Bayol, N., Bénédet, F., Bry, X., Dauby, G., Deblauwe, V.: Unveiling African rainforest composition and vulnerability to global change. *Nature*, 593, 90-94, <https://doi.org/10.1038/s41586-021-03483-6>, 2021.
- Roberts, D.A., Smith, M.O., Adams, J.B.: Green vegetation, nonphotosynthetic vegetation, and soils in AVIRIS data. *Remote Sens. Environ.*, 44, 255-269, [https://doi.org/10.1016/0034-4257\(93\)90020-X](https://doi.org/10.1016/0034-4257(93)90020-X), 1993.
- 680 Roberts, D.A., Gardner, M., Church, R., Ustin, S., Scheer, G., Green, R.O.: Mapping Chaparral in the Santa Monica Mountains Using Multiple Endmember Spectral Mixture Models. *Remote Sens. Environ.*, 65, 267-279, [https://doi.org/10.1016/S0034-4257\(98\)00037-6](https://doi.org/10.1016/S0034-4257(98)00037-6), 1998.
- Rogan, J., Franklin, J., Roberts, D.A.: A comparison of methods for monitoring multitemporal vegetation change using Thematic Mapper imagery. *Remote Sens. Environ.*, 80, 143-156, [https://doi.org/10.1016/S0034-4257\(01\)00296-6](https://doi.org/10.1016/S0034-4257(01)00296-6). 2002.
- 685 Schaaf, C., Wang, Z.: MCD43A4 MODIS/Terra+Aqua BRDF/Albedo Nadir BRDF Adjusted Ref Daily L3 Global - 500m V006. In: NASA EOSDIS Land Processes DAAC
- Sen, Kumar, P.: Estimates of the Regression Coefficient Based on Kendall's Tau. *Publications of the American Statistical Association*, 63, 1379-1389, <https://doi.org/10.1080/01621459.1968.10480934>, 1968.
- Small, C.: The Landsat ETM+ spectral mixing space. *Remote Sens. Environ.*, 93, 1-17, 690 <https://doi.org/10.1016/j.rse.2004.06.007>, 2004
- Small, C., Milesi, C.: Multi-scale standardized spectral mixture models. *Remote Sens. Environ.*, 136, 442-454, <https://doi.org/10.1016/j.rse.2013.05.024>, 2013.
- Smith, A.M.S., Drake, N.A., Wooster, M.J., Hudak, A.T., Holden, Z.A., Gibbons, C.J.: Production of Landsat ETM+ reference imagery of burned areas within Southern African savannahs: comparison of methods and application to MODIS. *Int. J. Remote Sens.*, 28, 2753-2775, <https://doi.org/10.1016/10.1080/01431160600954704>, 2007. 695
- Smith, M.O., Ustin, S.L., Adams, J.B., Gillespie, A.R.: Vegetation in deserts: I. A regional measure of abundance from multispectral images. *Remote Sens. Environ.*, 31, 1-26, [https://doi.org/10.1016/0034-4257\(90\)90074-V](https://doi.org/10.1016/0034-4257(90)90074-V), 1990.
- Smith, W.K., Dannenberg, M.P., Yan, D., Herrmann, S., Barnes, M. L., Barron-Gafford, G.A., Biederman, J. A, Ferrenberg, S., Fox, A.M., Hudson, A., Knowles, J.F., MacBean, N., Moore, D.J.P., Nagler, P.L., Reed S. 700 C., Rutherford, W.A., Scott, R. L., Wang, X., Yang, J.: Remote sensing of dryland ecosystem structure and function: Progress, challenges, and opportunities. *Remote Sens. Environ.*, 233, 111401, <https://doi.org/10.1016/j.rse.2019.111401>, 2019.
- Soheb, M., Ramanathan, A., Bhardwaj, A., Coleman, M., Rea, B. R., Spagnolo, M., Singh, S., and Sam, L.: Multitemporal glacier inventory revealing four decades of glacier changes in the Ladakh region, *Earth Syst. Sci. Data*, 14, 4171–4185, doi: 10.5194/essd-14-4171-2022, 2022.

- 705 Song, X., Hansen, M.C., Stehman, S.V., Potapov, P.V., Tyukavina, A., Vermote, E.F., Townshend, J.R.: Global land change from 1982 to 2016. *Nature*, 560, 639-643, <https://doi.org/10.1038/s41586-018-0411-9>, 2018.
- Sonnentag, O., Chen, J.M., Roberts, D.A., Talbot, J., Halligan, K.Q., Govind, A.: Mapping tree and shrub leaf area indices in an ombrotrophic peatland through multiple endmember spectral unmixing. *Remote Sens. Environ.*, 109, 342-360, <https://doi.org/10.1016/j.rse.2007.01.010>, 2007.
- 710 Sousa, D., Small, C.: Globally standardized MODIS spectral mixture models. *Remote Sens Lett*, 10, 1018-1027, <https://doi.org/10.1080/2150704X.2019.1634299>, 2019
- Sousa, D., Small, C.: Spectral mixture analysis as a unified framework for the remote sensing of evapotranspiration. *Remote Sensing*, 10(12), 1961, <https://doi.org/10.3390/rs10121961>, 2018.
- Stehman, S.V., Olofsson, P., Woodcock, C.E., Herold, M., Friedl, M.A.: A global land-cover validation data set, II:
- 715 Augmenting a stratified sampling design to estimate accuracy by region and land-cover class. *Int. J. Remote Sens.*, 33, 6975-6993, <https://doi.org/10.1080/01431161.2012.695092>, 2012
- Sun, D.: Detection of dryland degradation using Landsat spectral unmixing remote sensing with syndrome concept in Minqin County, China. *International Journal of Applied Earth Observation & Geoinformation*, 41, 34-45, <https://doi.org/10.1016/j.jag.2015.04.015>, 2015.
- 720 Sun, D., Zhang, P., Sun, Q., Jiang, W.: A dryland cover state mapping using catastrophe model in a spectral endmember space of OLI: a case study in Minqin, China. *Int. J. Remote Sens.*, 1-22, <https://doi.org/10.1080/01431161.2019.1580795>, 2019.
- Sun, Q., Sun, D: A global estimate of monthly vegetation and soil fractions from spatio-temporally adaptive spectral mixture analysis during 2001-2022. <https://doi.org/10.57760/sciencedb.13287>, 2023
- Sun, Q., Zhang, P., Sun, D., Liu, A., Dai, J.: Desert vegetation-habitat complexes mapping using Gaofen-1 WFV (wide field
- 725 of view) time series images in Minqin County, China. *Int. J. Appl. Earth Obs.*, 73, 522-534, <https://doi.org/10.1016/j.jag.2018.07.021>, 2018.
- Sun, Q., Zhang, P., Wei, H., Liu, A., You, S., Sun, D.: Improved mapping and understanding of desert vegetation-habitat complexes from intraannual series of spectral endmember space using cross-wavelet transform and logistic regression. *Remote Sens. Environ.*, 236, 111516. <https://doi.org/10.1016/j.rse.2019.111516>, 2020.
- 730 Sun, Q., Zhang, P., Jiao, X., Han, W., Sun, Y., Sun, D.: Identifying and understanding alternative states of dryland landscape: a hierarchical analysis of time series of fractional vegetation-soil nexuses in China's Hexi Corridor. *Landscape and urban planning*. 215,104225, <https://doi.org/10.1016/j.landurbplan.2021.104225>, 2021.

- Sun, Q., Zhang, P., Jiao, X., Lun, F., Dong, S., Lin, X., Li, X., Sun, D.: A Remotely Sensed Framework for Spatially-Detailed Dryland Soil Organic Matter Mapping: Coupled Cross-Wavelet Transform with Fractional Vegetation and Soil-Related Endmember Time Series. *Remote Sens.* 14, 1701. <https://doi.org/10.3390/rs14071701>, 2022.
- 735
- Suess, S., van der Linden, S., Okujeni, A., Griffiths, P., Leitão, P. J., Schwieder, M., & Hostert, P.: Characterizing 32 years of shrub cover dynamics in southern Portugal using annual Landsat composites and machine learning regression modeling. *Remote Sens. Environ.* 219, 353-364, <https://doi.org/10.1016/j.rse.2018.10.004>, 2018.
- Tong, X., Brandt, M., Yue, Y., Horion, S., Wang, K., De Keersmaecker, W., Tian, F., Schurgers, G., Xiao, X., Luo, Y., Chen, C., Myneni, R., Shi, Z., Chen, H., Fensholt, R. 2018. Increased vegetation growth and carbon stock in China karst via ecological engineering. *Nature Sustainability*, 1, 44-50, <https://doi.org/10.1038/s41893-017-0004-x>, 2021
- 740
- Wang, Q., Ding, X., Tong, X., Atkinson, P. M.: Spatio-temporal spectral unmixing of time-series images. *Remote Sens. Environ.*, 259, 112407, <https://doi.org/10.1016/j.rse.2021.112407>, 2021.
- Yan, K., Gao, S., Chi, H., Qi, J., Song, W., Tong, Y., Yan, G.: Evaluation of the vegetation-index-based dimidiate pixel model for fractional vegetation cover estimation. *IEEE Transactions on Geoscience and Remote Sensing*, 60, 1-14, <https://doi.org/10.1109/TGRS.2020.3048493>, 2021.
- 745
- Yu, Z., Jin, X., Miao, L., and Yang, X.: A historical reconstruction of cropland in China from 1900 to 2016, *Earth Syst. Sci. Data*, 13, 3203–3218, <https://doi.org/10.5194/essd-13-3203-2021>, 2021.
- Zemp, M., Huss, M., Thibert, E., Eckert, N., McNabb, R., Huber, J., Barandun, M., Machguth, H., Nussbaumer, S.U., Gärtner-Roer, I.: Global glacier mass changes and their contributions to sea-level rise from 1961 to 2016. *Nature*, 568, 382-386, <https://doi.org/10.1038/s41586-019-1071-0>, 2019.
- 750
- Zeng, Y., Hao, D., Park, T., Zhu, P., Huete, A., Myneni, R., Chen, M. (2023). Structural complexity biases vegetation greenness measures. *Nat. Ecol. Evol.*, 7, 1790-1798, <https://doi.org/10.1038/s41559-023-02187-6>, 2023.
- Zhang, C., Ma, L., Chen, J., Rao, Y., and Chen, X.: Assessing the impact of endmember variability on linear spectral mixture analysis (LSMA): a theoretical and simulation analysis. *Remote Sens. Environ.*, 235, 111471. <https://doi.org/10.1016/j.rse.2019.111471>, 2019.
- 755
- Zhang, X., Liu, L., Zhao, T., Gao, Y., Chen, X., Mi, J.: GISD30: global 30 m impervious-surface dynamic dataset from 1985 to 2020 using time-series Landsat imagery on the Google Earth Engine platform, *Earth Syst. Sci. Data*, 14, 1831–1856, <https://doi.org/10.5194/essd-14-1831-2022>, 2022.
- 760
- Zhang, Y., Foody, G. M., Ling, F., Li, X., Ge, Y., Du, Y., Atkinson, P. M.: Spatial-temporal fraction map fusion with multi-scale remotely sensed images. *Remote Sensing of Environment*, 213, 162-181, <https://doi.org/10.1016/j.rse.2018.05.010>, 2018.

Zhao, J., Li, J., Liu, Q., Xu, B., Mu, X., Dong, Y.: Generation of a 16 m/10-day fractional vegetation cover product over China based on Chinese GaoFen-1 observations: method and validation. *International Journal of Digital Earth*, 16, 4229-4246, <https://doi.org/10.1080/17538947.2023.2264815>, 2023

765 Zhao, M., Cheng, C., Zhou, Y., Li, X., Shen, S., and Song, C.: A global dataset of annual urban extents (1992–2020) from harmonized nighttime lights, *Earth Syst. Sci. Data*, 14, 517–534, <https://doi.org/10.5194/essd-14-517-2022>, 2022.

Zhu, Z., Piao, S., Myneni, R.B., Huang, M., Zeng, Z., Canadell, J.G., Ciais, P., Sitch, S., Friedlingstein, P., Arneeth, A.: Greening of the Earth and its drivers. *Nat Clim Change*, 6, 791-795, <https://doi.org/10.1038/nclimate3004>, 2016